



CHALMERS

Chalmers Publication Library

Fast Analysis of Periodic Antennas and Metamaterial-Based Waveguides

This document has been downloaded from Chalmers Publication Library (CPL). It is the author's version of a work that was accepted for publication in:

Computational Electromagnetics – Recent Advances and Engineering Applications

Citation for the published paper:

Maaskant, R. (2014) "Fast Analysis of Periodic Antennas and Metamaterial-Based Waveguides". Computational Electromagnetics – Recent Advances and Engineering Applications pp. 75-109.

http://dx.doi.org/10.1007/978-1-4614-4382-7_3

Downloaded from: <http://publications.lib.chalmers.se/publication/194108>

Notice: Changes introduced as a result of publishing processes such as copy-editing and formatting may not be reflected in this document. For a definitive version of this work, please refer to the published source. Please note that access to the published version might require a subscription.

Chalmers Publication Library (CPL) offers the possibility of retrieving research publications produced at Chalmers University of Technology. It covers all types of publications: articles, dissertations, licentiate theses, masters theses, conference papers, reports etc. Since 2006 it is the official tool for Chalmers official publication statistics. To ensure that Chalmers research results are disseminated as widely as possible, an Open Access Policy has been adopted. The CPL service is administrated and maintained by Chalmers Library.

(article starts on next page)

Fast Analysis of Periodic Antennas and Metamaterial-Based Waveguides

Rob Maaskant

1	Introduction	2
2	The Characteristic Basis Function Method (CBFM)	4
	2.1 Employing Characteristic Basis Functions (CBFs)	5
	2.2 Generation of CBFs	7
3	Fast Reduced Matrix Generation	11
	3.1 Exploiting Array Translation Symmetry	11
	3.2 The Adaptive Cross Approximation (ACA) Algorithm	15
4	Computation of Radiation and Impedance Characteristics	18
	4.1 Input Admittance Matrix	18
	4.2 Antenna Embedded Element Patterns	19
5	Multilevel CBFM	20
6	Numerical Results	21
	6.1 A 7×1 (Vivaldi) Tapered Slot Antenna Array	22
	6.2 CBFM – ACA Hybridization Results	25
	6.3 Multilevel CBFM – Array of Subarray Antennas	27
	6.4 A Metamaterial-Based Gap Waveguide	29
7	Summary	34
	References	35

Abstract A tailored version of the Characteristic Basis Function Method (CBFM) is presented as a matrix compression technique for the method-of-moments (MoM) to rapidly compute the impedance, radiation, and propagation characteristics of large periodic structures, including antenna arrays and metamaterial-based waveguides. The compression is achieved by employing physics-based Characteristic Basis Functions (CBFs), which are generated numerically and in a time-efficient manner by exploiting array symmetries. The supports of these CBFs partially overlap between electrically interconnected array elements to preserve the continuity of the surface current across common boundaries. The translation symmetry is also exploited to expedite

R. Maaskant
Chalmers University of Technology S-41296 Gothenburg, Sweden, e-mail: rob.maaskant@chalmers.se.

the meshing process of the structure, to construct the reduced matrix equation, and to rapidly compute the antenna radiation patterns. The Adaptive Cross Approximation (ACA) algorithm is applied to reduce the matrix fill-time even further. The numerical examples demonstrate high accuracy and excellent memory compressing capabilities of the considered method. Among the problems, we consider a very large array of nested subarray antennas employing more than 1E6 low-level basis functions, which is solved directly, in-core, through a multilevel CBFM approach, and we analyze a metamaterial-based gap waveguide through a CBFM-enhanced MoM approach employing the parallel-plate Green's function.

1 Introduction¹

Recent advances in computational electromagnetics (CEM) have enabled us to analyze large real-world antenna and scattering problems that were beyond our reach only a few years ago. In this chapter, we will provide only a limited overview of the literature that is closely related to the problem at hand, namely, fast analysis of large finite periodic structures, including antenna arrays and novel metamaterial-based waveguide structures analyzed through the Method-of-Moments (MoM, [14]).

Regarding the numerical analysis of finite periodic structures, asymptotic infinite-array approaches with corrections for the edge truncation effects have been developed, which are effective when the edge behavior of an array is local, and almost independent of the array size. This is true for very large arrays where the center elements behave as infinite-array elements. One can then solve for the fringe current describing the difference between the finite- and the associated infinite-array current [33]. The advantage is that the fringe current can be expanded by using relatively few basis functions, derived from a diffraction analysis of canonical structures, whose use requires the solution of only a moderately sized matrix equation. Other infinite-array-based techniques that expedite the finite array analysis can be found in [6, 8, 39, 44]. Infinite array approaches are particularly efficient if both the structure and fields are (nearly) periodic; otherwise, the method may not be the preferred choice. In fact, for moderate-sized arrays, and for those that require a high degree of flexibility in terms of array lattice geometry and element shape, it is preferable to use methods that are based on analyzing finite-size arrays.

One can employ subsectional basis functions of higher-order polynomials to reduce the size of the MoM matrix equation [11]; moreover, by employing macro basis functions an even greater reduction in the number of unknowns can be achieved. Since macro-domain functions can be constructed as fixed combinations of subsectional functions, these macro functions can conform to

¹ This chapter is largely based upon Maaskant's PhD dissertation [22].

arbitrarily shaped geometries. An additional advantage of using these macro basis functions is that existing codes can be reused with only minor modifications. These types of macro functions are sometimes referred to as aggregated basis functions, and have been applied to arrays of disconnected patch antennas in [47] and [15].

The expansion wave concept is also a method which reduces the number of unknowns without compromising the solution accuracy or geometrical flexibility of the low-level basis functions. It decomposes both the incident and scattered fields to and from an isolated array element in terms of only a few expansion functions [46]. This concept of reducing the matrix equation and decomposing the problem into smaller problems has been widely exploited in recently developed iterative-free methods for large-scale problems. For instance, the Characteristic Basis Function Method (CBFM) [24, 32, 34, 43, 49], which has been successfully applied to a large class of scattering and radiation problems, the Synthetic-Functions Approach (SFX) [29], [31], the Sub-Entire-Domain Basis Function Method (SED) [21], the eigencurrent approach [2], which has recently been combined with the Linear Embedding via Green's Operators approach (LEGO, [19]), and a subdomain multilevel approach [41]. The objectives of these methods are similar, namely to reduce the matrix equation by employing physics-based macro basis (and test) functions for the electric and/or magnetic surface currents.

In this chapter, we tailor the CBFM for the fast analysis of large periodic structures. We propose a dedicated array meshing method which exploits the array translation symmetry and preserves the quasi-Toeplitz symmetry in the reduced MoM matrix. Special attention is devoted to the problem of the efficient generation of a representative set of Characteristic Basis Functions (CBFs), and this is only done for a few unique array elements. Also, since the array elements may be electrically interconnected to one another, a post-windowing technique is developed to shape the initially generated CBFs in order to guarantee a piecewise continuous current flow at the interconnections by letting the CBFs partially overlap. This is an alternative method to [29], where one employs an additional independent set of "connection" basis functions to ensure the electrical connectivity between adjacent antenna elements. Hence, the herein presented overlapping domain decomposition method (DDM) requires less unknowns and therefore enables us to solve larger problems, although the method in [29] may provide a better continuity of the current in the interconnection regions.

We point out that the savings realized in CBFM, in terms of both memory and computation time, are significant; the solution time (for direct solvers) scales as $\mathcal{O}(N^3)$, where N now becomes a relatively small number associated with the total number of CBFs. The proportionality constant, however, slightly increases because of the additional time that is required to generate CBFs. The construction time of the reduced matrix scales as $\mathcal{O}(N^2)$, where N still represents the relatively large number of subsectional basis functions making up the CBFs, so that the fill-time of the reduced matrix governs

the total execution time. A number of hybrid methods have been proposed to reduce the matrix-fill time. For instance, in [40] the reaction integral between the macro basis and testing functions is computed using a suitable approximation. A generalization of this approach has led to the introduction of the Fast Multipole Method (FMM) for the rapid computation of these reactions [7], [11]. Alternatively, the Adaptive Integral Method (AIM) has also been applied to compute these reduced matrix entries efficiently [48], [3]. In the present chapter we generate the reduced matrix in a time-efficient manner by hybridizing the CBFM with the Adaptive Cross Approximation (ACA) algorithm. The ACA algorithm was originally developed for the rapid construction of the rank-deficient off-diagonal MoM matrix blocks [1, 18, 50]; however, it will be shown that the algorithm is also suited to compute the off-diagonal MoM blocks of the CBF-reduced matrix in a time-efficient manner. The ACA algorithm is purely algebraic in nature, kernel independent and relatively easy to implement. Furthermore, the algorithm does not require *a priori* knowledge of each MoM submatrix.

The above-described mathematical framework is supplemented with a methodology to rapidly compute the radiation and port impedance characteristics, and the multilevel CBFM is described as a generalization of the monolevel CBFM afterwards.

The accuracy of the method is assessed for a 7×1 array of Tapered Slot Antennas (TSAs). Their analyses constitutes a challenging numerical problem, since the outer edges of the TSA fins are (entirely) connected to the adjacent elements as a result of which the analysis of the entire array problem cannot be localized to the analysis of a single isolated TSA element. Following this, the numerical results are presented on the CBFM–ACA hybridization. This is followed up by the extremely large problem of solving large antenna arrays of nested disjoint subarrays, whose solution is found through the multilevel CBFM. Finally, we consider a low-loss low-cost novel class of waveguides: the so-called gap waveguides. Gap waveguides are metamaterial-based waveguides employing periodic textures of small metallic objects to emulate an artificial magnetic conductor, thereby exhibiting superior propagation characteristics to the more conventional waveguides. It is shown that the CBFM can handle these fine-feature structures with relative ease, even if the problem grows very large.

2 The Characteristic Basis Function Method (CBFM)

For the sake of completeness, we briefly review the CBFM in this section, though the method has also been discussed in a number of other chapters in this book for a variety of other problems for different applications, e.g., RCS computation and analysis of microwave integrated circuits.

2.1 Employing Characteristic Basis Functions (CBFs)

In algebraic terms, the objective of CBFM is to solve the large system of linear equations

$$\mathbf{Z}\mathbf{l} = \mathbf{v} \quad (1)$$

for the unknown coefficient vector \mathbf{l} in an iteration-free and time-efficient manner. The complex symmetric matrix \mathbf{Z} is of size $N \times N$ and assumed large enough to pose a severe computational burden on the memory storage and matrix fill times, let alone on the numerical solution of (1). This limitation can be overcome by CBFM, which is capable of solving the system directly for multiple right-hand-sides (MRHS) and in-core for N upwards of one million, or even larger, depending upon the computational platform.

The degrees of freedom (DoFs) of the solution vector \mathbf{l} in (1) is N . However, the solution vector tends to lie in a much smaller subspace for most practical EM problems that are solved through the method of moments (MoM) employing a fine discretization scheme. For instance, for a transmitting dipole antenna, the solution vector \mathbf{l} – representing the current in terms of N subsectional basis functions – most likely resembles a cosine-type of function. The actual dipole current can therefore be represented rather accurately through a very low number of linearly independent solution vectors, or macro basis functions – called Characteristic Basis Functions (CBFs) – resembling the cosine-type of functions. Hence, the key feature of CBFM is to reduce the DoFs of \mathbf{l} by two-to-three orders through a physics-based expansion such as:

$$\mathbf{l} = \sum_{q=1}^Q I_q^{\text{CBF}} \mathbf{J}_q^{\text{CBF}} \quad (2)$$

where $\{\mathbf{J}_q^{\text{CBF}}\}$ are the Q CBFs ($Q \ll N$), and $\{I_q^{\text{CBF}}\}$ are the corresponding CBF expansion coefficients. Substituting (2) in (1), yields

$$\sum_{q=1}^Q I_q^{\text{CBF}} \mathbf{Z} \mathbf{J}_q^{\text{CBF}} = \mathbf{v} \quad (3)$$

after which the error \mathbf{R} can be defined as $\mathbf{R} = \sum_{q=1}^Q I_q^{\text{CBF}} \mathbf{Z} \mathbf{J}_q^{\text{CBF}} - \mathbf{v}$. Weighting this error to zero using Q testing vectors $\{\mathbf{J}_p^{\text{CBF}}\}_{p=1}^Q$ that are identical to the Q CBFs (Galerkin's approach), gives

$$\sum_{q=1}^Q I_q^{\text{CBF}} \langle \mathbf{J}_p^{\text{CBF}}, \mathbf{Z} \mathbf{J}_q^{\text{CBF}} \rangle = \langle \mathbf{J}_p^{\text{CBF}}, \mathbf{v} \rangle \quad \text{for } p = 1, 2, \dots, Q, \quad (4)$$

where the symmetric dot-product $\langle \mathbf{a}, \mathbf{b} \rangle = \mathbf{a}^T \mathbf{b}$, and where the superscript T denotes the transposition operator. Eq. (4) represents a reduced matrix equation $\mathbf{Z}^{\text{red}} \mathbf{I}^{\text{CBF}} = \mathbf{V}^{\text{red}}$, where \mathbf{Z}^{red} is of size $Q \times Q$, whose matrix element $Z_{pq}^{\text{red}} = \langle \mathbf{J}_p^{\text{CBF}}, \mathbf{Z} \mathbf{J}_q^{\text{CBF}} \rangle$, and where the p th element of the $N \times 1$ RHS vector $\mathbf{V}_p^{\text{red}} = \langle \mathbf{J}_p^{\text{CBF}}, \mathbf{V} \rangle$.

Two major questions remain: (i) how to generate a representative set of CBFs (to be discussed in Sec. 2.2), and; (ii) how to rapidly generate the reduced matrix equation (4). Indeed, Eq. (4) contains computationally expensive matrix-vector products, and also requires constructing the original moment matrix \mathbf{Z} , both of which are both time-consuming tasks.

We can alleviate the burden of the matrix-vector multiplications as follows. Consider the example of a 7×1 singly-polarized TSA array in Fig. 1. The entire surface S supporting the surface current is triangulated, after

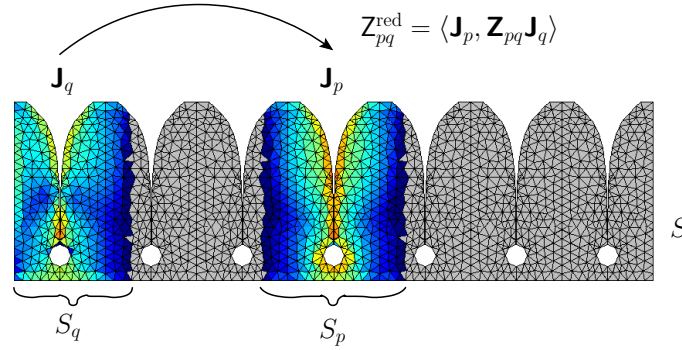


Fig. 1 Reduced matrix element Z_{pq}^{red} ; the dot product between the (observation) CBF \mathbf{J}_p and the excitation vector $\mathbf{Z}_{pq} \mathbf{J}_q$ due to the (source) CBF \mathbf{J}_q .

which pairs of triangles form N Rao-Wilton-Glisson (RWG) basis functions for modeling the current [35]. To rapidly compute the matrix element $Z_{pq}^{\text{red}} = \langle \mathbf{J}_p^{\text{CBF}}, \mathbf{Z} \mathbf{J}_q^{\text{CBF}} \rangle$ in (4), we note from Fig. 1 that if the supports of the CBFs are local – in this case about the size of a single antenna element – the CBFs will contain many zeros. Indeed, when squeezing out the zero entries, i.e., $\mathbf{J}_p^{\text{CBF}} \mapsto \mathbf{J}_p$ and $\mathbf{J}_q^{\text{CBF}} \mapsto \mathbf{J}_q$, effectively only the matrix block \mathbf{Z}_{pq} of \mathbf{Z} representing the interactions between the group pair of RWGs on the subdomains S_p and S_q need be computed, and we can write $Z_{pq}^{\text{red}} = \langle \mathbf{J}_p, \mathbf{Z}_{pq} \mathbf{J}_q \rangle$. Similarly, the zero entries in \mathbf{V} on the RHS can be discarded, so that $\mathbf{V}_q^{\text{red}} = \langle \mathbf{J}_p, \mathbf{V}_p \rangle$ in (4), where \mathbf{V}_p is a subset of \mathbf{V} pertaining to the local support S_p .

The final reduced matrix equation can be written as

$$\begin{bmatrix} \langle \mathbf{J}_1, \mathbf{Z}_{11} \mathbf{J}_1 \rangle & \langle \mathbf{J}_1, \mathbf{Z}_{12} \mathbf{J}_2 \rangle & \cdots & \langle \mathbf{J}_1, \mathbf{Z}_{1L} \mathbf{J}_L \rangle \\ \langle \mathbf{J}_2, \mathbf{Z}_{21} \mathbf{J}_1 \rangle & \langle \mathbf{J}_2, \mathbf{Z}_{22} \mathbf{J}_2 \rangle & \cdots & \langle \mathbf{J}_2, \mathbf{Z}_{2L} \mathbf{J}_L \rangle \\ \vdots & \vdots & \ddots & \vdots \\ \langle \mathbf{J}_L, \mathbf{Z}_{L1} \mathbf{J}_1 \rangle & \langle \mathbf{J}_L, \mathbf{Z}_{L2} \mathbf{J}_2 \rangle & \cdots & \langle \mathbf{J}_L, \mathbf{Z}_{LL} \mathbf{J}_L \rangle \end{bmatrix} \begin{bmatrix} \mathbf{I}_1^{\text{CBF}} \\ \mathbf{I}_2^{\text{CBF}} \\ \vdots \\ \mathbf{I}_L^{\text{CBF}} \end{bmatrix} = \begin{bmatrix} \langle \mathbf{J}_1, \mathbf{V}_1 \rangle \\ \langle \mathbf{J}_2, \mathbf{V}_2 \rangle \\ \vdots \\ \langle \mathbf{J}_L, \mathbf{V}_L \rangle \end{bmatrix} \quad (5)$$

where we now have assumed that the subdomain S_p can generally support more than one, say Q_p , CBFs, so that the Q_p columns in the matrix $\mathbf{I}_p^{\text{CBF}}$ are the expansion coefficient vectors for the CBFs on the p th subdomain. The total number of employed CBFs is therefore the sum of all the CBFs per subdomain, thus $Q = \sum_{p=1}^L Q_p$, where L is the total number of subdomains.

We observe that the CBFM can be thought of as a domain decomposition method (DDM), since the CBFs have a local support and need to be generated only for a smaller subproblem as detailed in the next section.

2.2 Generation of CBFs

Note that the supports of the CBFs in Fig. 1 slightly extend beyond the size of a single TSA element, so that the subdomains partially overlap. Such partial overlapping preserves the continuity of the surface current across the common boundaries between interconnected TSAs when CBFs are superimposed to form the spurious-free solution for \mathbf{I} in (1). This specific implementation is referred to as an overlapping DDM, although non-overlapping DDMs can be implemented as well that employ additional subsectional basis functions in order to mitigate the interface glitch effects [30].

While [24] presents a generic technique to generate the CBFs for arrays of electrically interconnected antenna elements, only the most widely used version of this technique will be considered hereafter. The procedure for generating the CBFs is explained in four stages below for the example depicted in Fig. 2.

Step I: Mesh generation

Only a single TSA element is triangulated and replicated at various element positions throughout the array lattice by means of geometrical translations. While rapidly generating the entirely meshed structure, the partitioning of RWGs is kept identical for each array element and the polarity of the RWGs that electrically interconnect the antenna elements is chosen consistently, and such that the entirely meshed array facilitates a one-to-one mapping of partially overlapping CBFs. This mapping of CBFs has been visualized in the transition from Step III to Step IV (see also Sec. 3.1 for more details).

Step II Generation of primary CBFs

Three subarrays are extracted from the entirely meshed array to generate the CBFs, i.e., two corner elements and one central element along with their electrically interconnected adjacent element(s). Since we are here interested

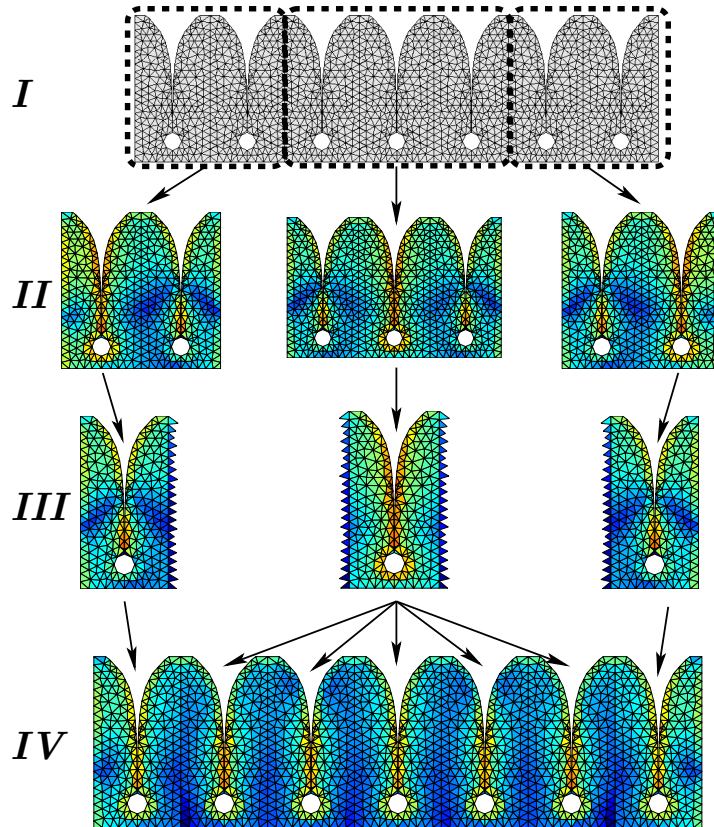


Fig. 2 Step I: fully meshed 7x1 TSA array; Step II: extraction of 3 subarrays for generating the CBFs; Step III: truncation of the subarray induced currents to form the CBFs; Step IV: mapping of CBFs onto the fully meshed array, constructing the reduced matrix equation (5), and the final synthesized surface current solution for broadside scan.

in computing the antenna impedance matrix and radiation patterns, we consider the problem on transmit, so that the primary CBFs are also generated on transmit to achieve an accurate representation of the current. These are generated by exciting each accessible port of the three subarrays sequentially. As a result, the number of primary generated CBFs equals the number of accessible ports for each subarray.

More specifically, suppose that for one of the subarrays in Step II, the current on a subarray is expanded into N_{sub} RWG basis functions, then the subarray currents are found by solving a small matrix equation for the MRHS $N \times K$ column-augmented excitation matrix \mathbf{V}_{sub} , i.e.,

$$\mathbf{I}_{\text{sub}} = \mathbf{Z}_{\text{sub}}^{-1} \mathbf{V}_{\text{sub}} \quad (6)$$

where \mathbf{Z}_{sub} is the moment matrix of the corresponding subarray RWGs, and the K columns of the matrix \mathbf{I}_{sub} are the induced currents when exciting the ports of the subarrays. As a result, two primary CBFs are generated on the outer two subarrays, while three CBFs are generated on the inner subarray.

It should be pointed out that, when analyzing the entire structure as a scattering problem, one is typically interested in its response to a series of plane waves incident from various directions. Hence, it is natural to also let a plane-wave spectrum (PWS) be incident on each subarray for generating the initial set of CBFs. Although this is an obvious choice for scattering problems, antenna array problems have been analyzed successfully using the PWS-generated CBFs as well, both for the receive and transmit cases [23].

Step IIIa *Truncation and Post-Windowing of CBFs*

Next, we apply a trapezoidal windowing function $\mathbf{\Lambda}$ to each of the sets of CBFs that were generated for the subarrays in Fig. 2, Step II, in order to arrive at Step III, where the spurious edge-singular currents arising from subarray truncation effects have been eliminated [24]. In particular, we will employ a pulse windowing function to reduce the support of each CBF to the size of one antenna element only, while retaining possible “connection” RWGs. Note the one-cell overlap in Step III at connecting boundaries where indeed no edge truncation effects are visible.

For each subarray, the final windowed set of CBFs \mathbf{J}_{sub} (Step III, Fig. 2) is thus computed as

$$\mathbf{J}_{\text{sub}} = \mathbf{\Lambda} \mathbf{I}_{\text{sub}} = \mathbf{\Lambda} \mathbf{Z}_{\text{sub}}^{-1} \mathbf{V}_{\text{sub}} \quad (7)$$

where the diagonal matrix $\mathbf{\Lambda}$ post-multiplies the RWGs in the initial set of CBFs \mathbf{I}_{sub} either by 0, 1/2, or 1, depending upon whether they are in the external, overlap, or internal region of the resulting truncated subdomain, respectively. Note that the “connection” RWGs in the overlap region are colored bluish as a result of weighting these RWGs by 1/2, while the zeros in \mathbf{J}_{sub} are discarded to truncate the support. The RWGs are weighted by 1/2 to make sure that, when adjacent CBFs are superimposed, the sum of the weights of each pair of overlapping RWGs amounts to unity again. If three conductors are connected, one has to multiply by 1/3, and so on.

Step IIIb *Reducing the number of CBFs by using the SVD*

To obtain a well-conditioned reduced moment matrix in (5), it is necessary that the CBFs be linearly independent, which can be assured through a Singular Value Decomposition (SVD) operation as this renders the CBFs orthogonal.

Let the matrix \mathbf{J}_q be of size $N_q \times K_q$, where N_q and K_q denote the total number of RWGs and the number of initially generated CBFs on the q th subdomain, respectively. Upon invoking the SVD, \mathbf{J}_q is decomposed as

$$\mathbf{J}_q = \mathbf{U}\mathbf{D}\mathbf{Q}^H \quad (8)$$

where \mathbf{U} is an $N_q \times K_q$ matrix with orthonormal columns/CBFs [45, p. 27]; \mathbf{Q} is a $K_q \times K_q$ unitary matrix; and, \mathbf{D} is a $K_q \times K_q$ diagonal matrix of the form $\text{diag}(\sigma_1, \sigma_2, \dots, \sigma_{K_q})$. The non-negative real-valued diagonal entries of \mathbf{D} can be required to be ordered as $\sigma_1 \leq \sigma_2 \leq \dots \leq \sigma_{K_q}$ and are the singular values of \mathbf{J}_q . The presence of singular values of zero, or near-zero, indicates that the matrix is singular or ill-conditioned. Therefore, to improve this condition number, a thresholding procedure is used on the normalized singular values

$$R_n = \frac{\sigma_n}{\sigma_{max}} \quad n = 1, 2, \dots, K_q. \quad (9)$$

Each of these normalized quantities is compared to an appropriate threshold, and the corresponding singular value is set to zero if this level is smaller than the specified threshold. Suppose this happens for $n > N_\sigma$, then the first N_σ left singular vectors of \mathbf{U} forms the orthonormal set of CBFs that are retained.

Step IIIc Generation of Secondary CBFs

The accuracy of the final solution for the current can be increased further by accounting for the mutually coupled subdomains in a more detailed manner through employing additional higher-order CBFs. Then, the primary CBFs \mathbf{J}_q , which are supported by the q th subdomain are, in turn, used as distant current sources to the subarrays shown in Step II (Fig. 2) to mimic possible surface currents on neighboring array elements that are located within a certain electrical distance from the subarray under excitation. Following (6), the currents \mathbf{J}_{sub} on a subarray are then computed as

$$\mathbf{I}_{\text{sub}} = \mathbf{Z}_{\text{sub}}^{-1} \mathbf{V}_{\text{sub}} = \mathbf{Z}_{\text{sub}}^{-1} \mathbf{Z}_{\text{sub},q} \mathbf{J}_q \quad (10)$$

where $\mathbf{Z}_{\text{sub},q}$ is the moment matrix block between the RWGs on the q th source domain, which supports a set of primary source CBFs \mathbf{J}_q , and the RWGs on the subarray under excitation. Accordingly, the CBF support is truncated by using (7), appended to the existing set of primary CBFs, and then we follow this up with an SVD orthogonalization-thresholding procedure. If the combined set of initially generated primary and secondary CBFs is sufficiently small, it is sufficient to perform the SVD only once. However, a multi-stage SVD procedure has been found to be more efficient in most cases, also for scattering problems where the primary CBFs are typically generated by using a PWS approach [10].

The total number of initially-generated secondary CBFs depends upon the total number of distant subdomains that are considered within a certain radius from the subarray under excitation. To increase the number of CBFs, one can also generate tertiary CBFs from the primary and secondary ones. However, at some point the SVD prevents us from adding more CBFs that are not sufficiently independent of the existing set of CBFs. Hence, convergence

of the solution depends upon the final solution accuracy desired, and this is controllable through the choice of the SVD threshold.

Step IV Mapping of CBFs and solving for the current

After retaining a relatively small set of CBFs for each truncated subdomain (Step III, Fig. 2), the CBFs are mapped onto the various subdomains throughout the entire array (Step IV, Fig. 2). Afterwards, the reduced matrix equation in Eq. (5) is constructed and solved directly for MRHS without resorting to iterative techniques. The resulting surface current for the 7×1 TSA array is shown in Fig. 2 for a broadside scan, when all the elements are excited by a voltage source across the slotline section.

3 Fast Reduced Matrix Generation

3.1 Exploiting Array Translation Symmetry

The reduced moment matrix \mathbf{Z}^{red} in (5) can be constructed efficiently by exploiting the translation symmetry between CBFs. As an example, Fig. 3 graphically exemplifies that the reduced matrix block $\mathbf{Z}_{pq}^{\text{red}}$ equals $\mathbf{Z}_{p+1;q+1}^{\text{red}}$, because both blocks represent reactions between identical, though translated, set of CBFs. It follows that,

$$\mathbf{Z}_{pq}^{\text{red}} = \langle \mathbf{J}_p, \mathbf{Z}_{pq} \mathbf{J}_q \rangle = \langle \mathbf{J}_{p+1}, \mathbf{Z}_{p+1;q+1} \mathbf{J}_{q+1} \rangle = \mathbf{Z}_{p+1;q+1}^{\text{red}} \quad (11)$$

provided that both S_q and S_p [see Fig. 3(a)] support sets of CBFs that map one-to-one onto the one-element translated subdomains S_{q+1} and S_{p+1} [see Fig. 3(b)], respectively, using the same translation vector. Hence, to fully exploit translation symmetry, the periodic structure must be discretized in a specific manner to facilitate this CBF mapping and, hence, a consistent triangulation and partitioning of the RWGs of all subdomains (and thus array elements) is required as further clarified below.

The entire array mesh can be efficiently constructed from a few elementary meshed array elements, called the base elements, see for instance the bowtie element in Fig. 4 (Step I). The geometry of each base element is discretized by a number of polygonal facets of which the outlines are described by a set of boundary nodes (black dots). Here, the bowtie base element comprises of 3 polygonal surfaces, i.e., two triangular fins and one small port polygon connecting the fins. Each planar polygonal facet is supplied by a non-uniform grid of internal nodes and subsequently triangulated in a 2-D plane by using a Delaunay meshing routine [4, 9]. The internal grid is distributed such that the elementary triangles are very nearly equilateral. Subsequently, nodes and triangles are added along the boundaries to ensure that the triangulations would be consistent with those of the electrically interconnected adjacent elements when these base elements are placed in the array environment. Next,

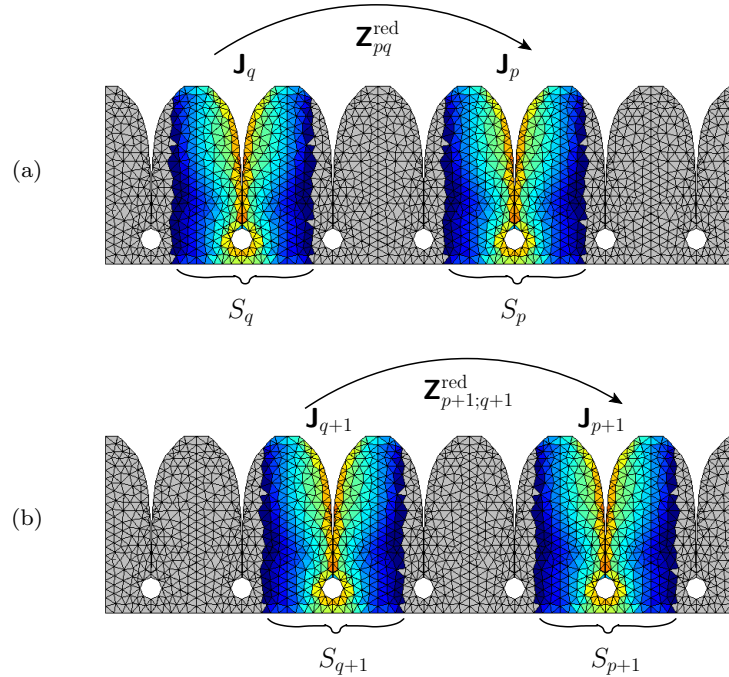


Fig. 3 Construction of identical reduced matrix blocks Z_{pq}^{red} and $Z_{p+1;q+1}^{\text{red}}$.

triangulated base elements are equipped with the RWGs. Step I (Fig. 4) shows a possible RWG polarity distribution, visualized by vectors that join the common edges of each pair of triangles to form an RWG.

Step II illustrates a one-to-one replication of the discretized base element at array element locations $r_1 \dots r_5$. Note that, at this stage, the RWGs ensuring the electrical connection between array elements have not yet been established. This is accomplished in Step III, where the triangles along a connection line are separately equipped with RWGs and subsequently mapped (recursively) onto the various corresponding connection lines that remain to be equipped with RWGs. For this purpose, we utilize the array symmetry as detailed below. A pseudo Matlab code of the recursive-mapping algorithm is included in the appendix of [26]. Finally, a full meshing of the array geometry (Step IV) facilitates a one-to-one mapping of the CBFs, even though each supporting subdomain extends beyond the outer boundaries of an array element, as shown in Fig. 3.

Next, the translation symmetry between identical pairs of CBFs can be determined. Following the generation of the boundary nodes for the array in a manner shown in Fig. 4, Step II, where we replicate the boundary nodes of the base antenna element(s) at their respective array positions, we can determine which array elements are electrically interconnected. Furthermore, when

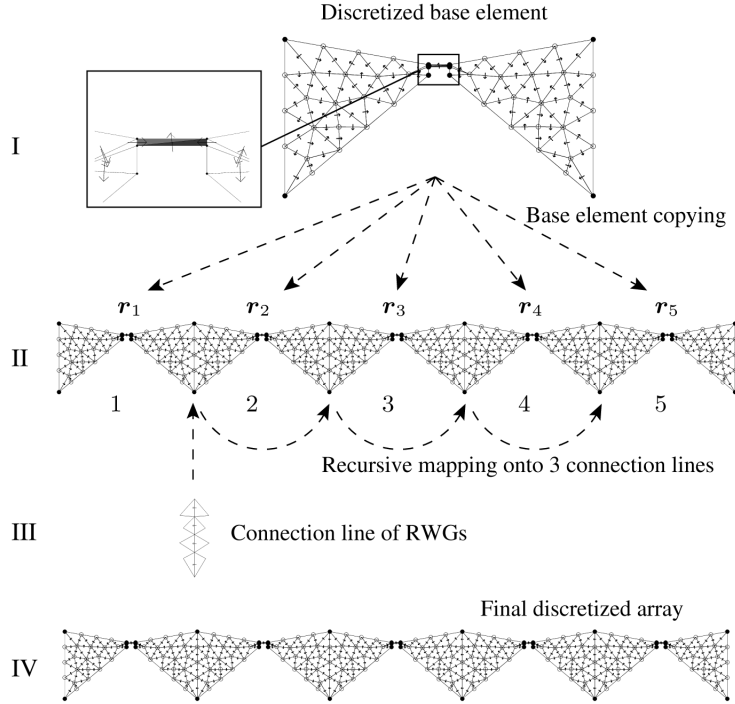


Fig. 4 Efficient and consistent meshing of the antenna array structure to fully exploit translation symmetry.

using multiple base elements, such as in the case of dual-polarized arrays, one can also keep track of the type of base element that is interconnected. Let the element interconnection and the corresponding base element type be stored in two separate matrices. Then, for our example, using only one type of base element (the bowtie element in Fig. 4, Step I), we have:

$$\begin{pmatrix} 1 & 2 & 0 \\ 2 & 1 & 3 \\ 3 & 2 & 4 \\ 4 & 3 & 5 \\ 5 & 4 & 0 \end{pmatrix} \quad \text{and} \quad \begin{pmatrix} 1 & 1 & 0 \\ 1 & 1 & 1 \\ 1 & 1 & 1 \\ 1 & 1 & 1 \\ 1 & 1 & 0 \end{pmatrix} \quad (12)$$

where the first rows of the left- and right-hand matrices indicate that antenna element 1 is connected to antenna element 2, and that they are both base elements of type-1 (ignore the zero entries), and so forth.

Also, for each array element, one can determine the relative positions of the electrically interconnected elements surrounding it. Upon comparing the groups of relative position vectors in conjunction with the corresponding

base element types (rows of second matrix), one can readily determine which subdomains (and therefore corresponding set of CBFs) are identical. For our example, subdomains $\{2, 3, 4\}$; $\{1\}$; and $\{5\}$ form the 3 unique groups. We need to only generate one set of CBFs per unique subdomain, in this case for subdomains 1, 5 and 3, where subdomain 3 is chosen from the first group as the most central element. Elements 1, 5 and 3 are extracted from the fully meshed array, together with their neighboring array elements (within a specified radius), to form the resulting three subarrays that are used to generate the CBFs. After windowing these CBFs, the CBFs supported by subdomain 3 are mapped onto the subdomains 2, 3, and 4.

After determining the unique subdomains (1, 5 and 3), from which the CBFs are mapped, we also compute the relative element array position vectors between all array elements and store these in matrix form. For our example, we have

$$\begin{pmatrix} \mathbf{r}_1 - \mathbf{r}_1 & 1 & 1 \\ \mathbf{r}_1 - \mathbf{r}_2 & 1 & 3 \\ \mathbf{r}_1 - \mathbf{r}_3 & 1 & 3 \\ \vdots & \vdots & \vdots \\ \mathbf{r}_5 - \mathbf{r}_3 & 5 & 3 \\ \mathbf{r}_5 - \mathbf{r}_4 & 5 & 3 \\ \mathbf{r}_5 - \mathbf{r}_5 & 5 & 5 \end{pmatrix} \quad (13)$$

where the first column holds the 25 relative array position vectors between element pairs, and the last two columns denote the corresponding two array elements that support the same set of CBFs from which they were initially mapped, namely either 1, 3 or 5. By comparing the rows, one can readily determine which subdomain pairs are identical in terms of the sets of CBFs supported by them (last two columns), as well as their mutual orientation and separation distance (first column). Upon selecting the unique rows, the minimal number of impedance matrix blocks that need to be filled can be determined (out of the 25 possible combinations). For convenience, we create a new matrix showing how the reduced matrix is built up from only a limited number of unique matrix blocks. For our example, the structure of the 5×5 block matrix is:

$$\begin{array}{c}
\text{Subdomain\#} \\
\mathbf{1} \\
\mathbf{2} \\
\mathbf{3} \\
\mathbf{4} \\
\mathbf{5}
\end{array}
\begin{array}{c}
\mathbf{1} \ \mathbf{2} \ \mathbf{3} \ \mathbf{4} \ \mathbf{5} \\
\left(\begin{array}{ccccc}
1 & 2 & 3 & 4 & 5 \\
& 6 & 7 & 8 & 9 \\
& & 6 & 7 & 10 \\
& & & 6 & 11 \\
& & & & 12
\end{array} \right)
\end{array}
\tag{14}$$

where 12 out of 25 non-redundant mutual impedance blocks have been identified, since we also exploited reciprocity (only the upper triangular part of the matrix is required). Note that, for this example, the matrix entry 7 denotes that the reactions between the CBFs supported by subdomains (antenna elements) 2 and 3 are identical to the reactions between the CBFs supported by the subdomains 3 and 4, as we can verify from Fig. 4. In conclusion, symmetry can be exploited for arrays of electrically interconnected elements to reduce the complexity of the matrix-filling process. For the present example of a regular-spaced single-polarized antenna array (Fig. 4), it can be shown that the computational complexity becomes linear when the translation symmetry is exploited.

3.2 The Adaptive Cross Approximation (ACA) Algorithm

If we exploit the quasi-Toeplitz structure in Eq. (5), we would only need to construct relatively few of these matrix blocks and reduce the matrix fill-time. The matrix fill-time can be further reduced as explained below. It is interesting to note that (5) suggests that a full matrix block \mathbf{Z}_{pq} has to be built before its compressed version $\langle \mathbf{J}_p, \mathbf{Z}_{pq} \mathbf{J}_q \rangle$ can be computed. Since \mathbf{Z}_{pq} is rank deficient, if this matrix block represents the interactions between a distant group pair of RWGs, we can write:

$$\mathbf{Z}_{pq}^{\text{red}} = \langle \mathbf{J}_p, \mathbf{Z}_{pq} \mathbf{J}_q \rangle \approx \langle \mathbf{J}_p, \tilde{\mathbf{Z}}_{pq} \mathbf{J}_q \rangle
\tag{15}$$

where $\tilde{\mathbf{Z}}_{pq}$ is a low-rank decomposition of \mathbf{Z}_{pq} , factorized in terms of a few relatively small sub-matrices².

The degree of rank deficiency of \mathbf{Z}_{pq} depends on the electrical distance that separates the observation and source groups p and q , as well as their sizes and mutual orientations [25]. The effective rank decreases for an increasingly larger separation distance. For well-separated groups of RWGs, the voltage excitation vector at the observation group p , produced by any source RWG,

² Alternatively, in [48], each column of the matrix product $\mathbf{Z}_{pq} \mathbf{J}_q$ is computed efficiently as an AIM matrix vector product.

can be expressed as a linear combination of the voltage vectors resulting from only a few of these source RWGs (source sampling). Likewise, the voltage excitation vector at the observation group p produced by any source RWG can be expressed as a linear combination of the voltage vectors of a few of these observation RWGs (field sampling). Hence, a cross-approximation technique can be used to adaptively construct the subsets of relevant source and observation RWGs.

In this work, we employ the Adaptive Cross Approximation (ACA) algorithm [1, 18, 50], which is an adaptive and on-the-fly rank-revealing block factorization of the rank-deficient sub-matrices. The ACA algorithm is purely algebraic in nature, and can be used irrespectively of the nature of the kernel of the integral equation, or the the basis functions or type of integral equation formulation. This makes the ACA algorithm attractive for handling problems involving arbitrary geometries and therefore suits the CBFM paradigm. In addition, the ACA algorithm only requires a partial knowledge of the original matrix and belongs to a large group of fast integral equation algebraic methods (see [50], and references therein). It has been shown that for low-frequency EMC problems of moderate electrical size both the memory and CPU time requirements for the ACA algorithm scale as $N^{4/3} \log N$ [50].

The ACA algorithm approximates $\tilde{\mathbf{Z}}_{pq}$ through the following block factorization

$$\tilde{\mathbf{Z}}_{pq} = \mathbf{U}_p^{N_p \times \text{rk}} \mathbf{V}_q^{\text{rk} \times N_q} = \sum_{i=1}^{\text{rk}} \mathbf{u}_i^{N_p \times 1} \mathbf{v}_i^{1 \times N_q} \quad (16)$$

where rk is a short-hand notation for $\text{rk}(\tilde{\mathbf{Z}}_{pq})$, which denotes the effective rank of the matrix $\tilde{\mathbf{Z}}_{pq}$. Further, $\mathbf{U}_p^{N_p \times \text{rk}}$ is a column-augmented matrix of size $N_p \times \text{rk}$, and $\mathbf{V}_q^{\text{rk} \times N_q}$ is a row-augmented matrix of size $\text{rk} \times N_q$. The i th column vector of \mathbf{U} and the i th row vector of \mathbf{V} are denoted by \mathbf{u}_i and \mathbf{v}_i , respectively. It is evident that, instead of storing the full matrix $\tilde{\mathbf{Z}}_{pq}$ of size $N_p \times N_q$, the algorithm requires the storage of only $(N_p + N_q) \times \text{rk}$ matrix entries. Also, the CPU time scales as $\mathcal{O}(\text{rk}^2(N_p + N_q))$. The ACA algorithm should not be used when subdomains either overlap fully ($p = q$), or partially. This is because, for these cases, the sub-matrices are diagonally dominant and, hence, seldom rank-deficient. For these cases, the computational overhead of the ACA algorithm becomes too high, so that a direct matrix-fill approach is preferred.

Finally, upon combining (15) and (16), the matrix $\mathbf{Z}_{pq}^{\text{red}}$ is efficiently computed by using

$$\mathbf{Z}_{pq}^{\text{red}} \approx \langle \mathbf{J}_p, \mathbf{U}_p \mathbf{V}_q \mathbf{J}_q \rangle. \quad (17)$$

Construction of the low-rank sub-matrices

The ACA algorithm constructs \mathbf{U}_p and \mathbf{V}_q by successively selecting rows and columns of the original matrix \mathbf{Z}_{pq} (source and field sampling). When

doing so, the approximate error matrix is constructed, given by $\|\tilde{\mathbf{R}}\|_F = \|\mathbf{Z}_{pq} - \tilde{\mathbf{Z}}_{pq}\|_F$, where $\|\cdot\|_F$ denotes the Frobenius norm, which is defined as the square root of the sum of the absolute squares of its matrix elements [12]. Furthermore, each time a new row or column of \mathbf{Z}_{pq} is selected, the corresponding error vector (row or column) is computed. This is done by subtracting the actual row or column vector from the corresponding row or column vector of the approximate matrix that has been constructed in the previous iteration. The row to be selected next corresponds to the index where the largest entry of the last computed error column is located. Likewise, the column to be selected next corresponds to the index where the largest entry of the last computed error row is located. After terminating the iterative process, the columns of \mathbf{U}_p are the successively computed error columns, whereas the rows of \mathbf{V}_q are the successively computed error rows. Furthermore, each row vector in \mathbf{V}_q is normalized by the maximum element of the last computed error column.

If the coupling matrix \mathbf{Z}_{pq} is of size $M \times N$, convergence of the ACA is guaranteed after $\min(M, N)$ iterations, since all its rows and columns have then been selected/computed previously and are thus reconstructed exactly [50]. The ACA does not exploit the oscillatory nature of the kernel in the integral equations, and may therefore not be as efficient as the multipole approaches. However, for many practical applications, especially for those with moderate electrical sizes, it is found that the ACA algorithm outperforms the Fast Multipole Method (FMM), particularly with multiple right-hand-side excitations [50]. For any case, to gain an appreciable speed advantage relative to a direct matrix fill method, the ACA algorithm should be terminated ahead, e.g. after rk iterations with $\text{rk} \ll \min(M, N)$, or when

$$\|\mathbf{R}\|_F \leq \kappa \|\mathbf{Z}_{pq}\|_F \quad (18)$$

for a given tolerance κ . Because the number of iterations depends on the chosen tolerance κ , it readily determines the effective rank of \mathbf{Z}_{pq} . Since \mathbf{Z}_{pq} is only partially known, the norm of \mathbf{R} is estimated after the k th iteration as

$$\|\mathbf{R}^{(k)}\|_F \approx \|\mathbf{u}_k\|_F \|\mathbf{v}_k\|_F. \quad (19)$$

Also, we can write

$$\begin{aligned} \|\mathbf{Z}_{pq}^{(k)}\|_F^2 &\approx \|\tilde{\mathbf{Z}}_{pq}^{(k)}\|_F^2 = \|\mathbf{U}_p^{(k)} \mathbf{V}_q^{(k)}\|_F^2 \\ &= \|\tilde{\mathbf{Z}}^{(k-1)}\|_F^2 + 2 \sum_{j=1}^{k-1} |\mathbf{u}_j^T \mathbf{u}_k| \cdot |\mathbf{v}_j \mathbf{v}_k^T| + \|\mathbf{u}_k\|_F^2 \|\mathbf{v}_k\|_F^2 \end{aligned} \quad (20)$$

where (20) is a recursive formula in terms of k .

Finally, we present the steps for code implementation of the ACA algorithm. Let the original matrix \mathbf{Z} be of size $M \times N$. In addition, let $\mathbf{I}^{\text{row}} = [I_1^{\text{row}}, I_2^{\text{row}}, \dots, I_{\text{rk}}^{\text{row}}]$ and $\mathbf{I}^{\text{col}} = [I_1^{\text{col}}, I_2^{\text{col}}, \dots, I_{\text{rk}}^{\text{col}}]$ be the arrays con-

taining orderly selected row and column indices of \mathbf{Z} , The vector \mathbf{u}_k represents the k th column of the matrix \mathbf{U} , and \mathbf{v}_k denotes the k th row of the matrix \mathbf{V} . In Matlab's notation, $\mathbf{R}(I_1^{\text{row}}, :)$ indicates the I_1^{row} th row of matrix \mathbf{R} . $\tilde{\mathbf{Z}}^{(k)}$ is the matrix $\tilde{\mathbf{Z}}$ at the k th iteration. Then, in pseudo-Matlab code, the algorithm is summarized as follows [50]:

Initialization ($k = 1$):

1. Initialize the 1st row index $I_1^{\text{row}} = 1$ and set $\tilde{\mathbf{Z}} = \mathbf{0}$.
2. Initialize the 1st row of the approx. error matrix: $\tilde{\mathbf{R}}(I_1^{\text{row}}, :) = \mathbf{Z}(I_1^{\text{row}}, :)$.
3. Find the 1st column index $I_1^{\text{col}} : |\tilde{\mathbf{R}}(I_1^{\text{row}}, I_1^{\text{col}})| = \max_j (|\tilde{\mathbf{R}}(I_1^{\text{row}}, j)|)$.
4. $\mathbf{v}_1 = \tilde{\mathbf{R}}(I_1^{\text{row}}, :)/\tilde{\mathbf{R}}(I_1^{\text{row}}, I_1^{\text{col}})$.
5. Initialize the 1st column of the approx. error matrix: $\tilde{\mathbf{R}}(:, I_1^{\text{col}}) = \mathbf{Z}(:, I_1^{\text{col}})$.
6. $\mathbf{u}_1 = \tilde{\mathbf{R}}(:, I_1^{\text{col}})$.
7. $\|\tilde{\mathbf{Z}}^{(1)}\|_F^2 = \|\mathbf{u}_1\|_F^2 \|\mathbf{v}_1\|_F^2$.
8. Find the 2nd row index $I_2^{\text{row}} : |\tilde{\mathbf{R}}(I_2^{\text{row}}, I_1^{\text{col}})| = \max_i (|\tilde{\mathbf{R}}(i, I_1^{\text{col}})|), i \neq I_1^{\text{row}}$.

k th iteration:

1. Update the I_k^{row} th row of $\tilde{\mathbf{R}}$: $\tilde{\mathbf{R}}(I_k^{\text{row}}, :) = \mathbf{Z}(I_k^{\text{row}}, :) - \sum_{l=1}^{k-1} (\mathbf{u}_l)_{I_k^{\text{row}}} \mathbf{v}_l$.
2. Find the k th column index $I_k^{\text{col}} : |\tilde{\mathbf{R}}(I_k^{\text{row}}, I_k^{\text{col}})| = \max_j (|\tilde{\mathbf{R}}(I_k^{\text{row}}, j)|), j \neq I_1^{\text{col}}, \dots, I_{k-1}^{\text{col}}$.
3. $\mathbf{v}_k = \tilde{\mathbf{R}}(I_k^{\text{row}}, :)/\tilde{\mathbf{R}}(I_k^{\text{row}}, I_k^{\text{col}})$.
4. Update the I_k^{col} th column of $\tilde{\mathbf{R}}$: $\tilde{\mathbf{R}}(:, I_k^{\text{col}}) = \mathbf{Z}(:, I_k^{\text{col}}) - \sum_{l=1}^{k-1} (\mathbf{v}_l)_{I_k^{\text{col}}} \mathbf{u}_l$.
5. $\mathbf{u}_k = \tilde{\mathbf{R}}(:, I_k^{\text{col}})$.
6. $\|\tilde{\mathbf{Z}}^{(k)}\|_F^2 = \|\tilde{\mathbf{Z}}^{(k-1)}\|_F^2 + 2 \sum_{j=1}^{k-1} |\mathbf{u}_j^T \mathbf{u}_k| |\mathbf{v}_j^T \mathbf{v}_k| + \|\mathbf{u}_k\|_F^2 \|\mathbf{v}_k\|_F^2$.
7. Check convergence, if $\|\mathbf{u}_k\|_F \|\mathbf{v}_k\|_F \leq \epsilon \|\tilde{\mathbf{Z}}^{(k)}\|_F$, end iteration.
8. Find the next row index $I_{k+1}^{\text{row}} : |\tilde{\mathbf{R}}(I_{k+1}^{\text{row}}, I_k^{\text{col}})| = \max_i (|\tilde{\mathbf{R}}(i, I_k^{\text{col}})|), i \neq I_1^{\text{row}}, \dots, I_k^{\text{row}}$.

4 Computation of Radiation and Impedance Characteristics

4.1 Input Admittance Matrix

In most MoM formulations, the input admittance matrix can be conveniently calculated, without additional manipulations, by using the induced surface currents when the ports are excited by voltage sources, while all other terminals are short-circuited. The mutual admittance (or impedance) between two

accessible ports a and b can be computed in terms of a reaction integral, and is variational in nature [13, pp. 118–119, 348–349]. Suppose \mathbf{J}^a is the induced surface current resulting from a voltage source of amplitude V_a exciting terminal a , while all other terminals are short-circuited. Likewise, \mathbf{J}^b is a result of exciting terminal b with V_b , while all other terminals are short-circuited. A stationary formula for the mutual input admittance Y_{ab}^{in} is given by

$$Y_{ab}^{\text{in}} = \frac{-1}{V_a V_b} \iint_{S_a} \mathbf{E}(\mathbf{J}^b) \cdot \mathbf{J}^a \, dS, \quad (21)$$

where $\mathbf{E}(\mathbf{J}^b)$ is the electric field radiated by \mathbf{J}^b , after which this field is weighted over the support S_a through \mathbf{J}^a . Upon expanding the surface current in terms of Q CBFs, we can write

$$\mathbf{J}^i(\mathbf{r}) = \sum_{q=1}^Q I_{q;i}^{\text{CBF}} \mathbf{J}_q^{\text{CBF}}(\mathbf{r}), \quad i \in \{a, b\}. \quad (22)$$

Next, we substitute (22) in (21) to obtain

$$Y_{ab}^{\text{in}} = \frac{-1}{V_a V_b} \sum_{p=1}^Q \sum_{q=1}^Q I_{p;a}^{\text{CBF}} \left[\iint_{S_a} \mathbf{E}(\mathbf{J}_{q;b}^{\text{CBF}}) \cdot \mathbf{J}_{p;a}^{\text{CBF}} \, dS \right] I_{q;b}^{\text{CBF}} \quad (23)$$

where we have used linearity to superimpose the EM fields. Equation (23) can be compactly rewritten in terms of matrix-vector products as

$$Y_{ab}^{\text{in}} = \frac{-1}{V_a V_b} \left\langle \mathbf{I}_a^{\text{CBF}}, \mathbf{Z}^{\text{red}} \mathbf{I}_b^{\text{CBF}} \right\rangle \quad (24)$$

which shows that each entry of the input admittance matrix can be expressed in terms of the reduced matrix \mathbf{Z}^{red} and the expansion coefficients for the CBFs $\mathbf{I}_i^{\text{CBF}}$. If desired, the input impedance matrix can be obtained by inverting the admittance matrix, or be transformed to an S -parameter matrix.

4.2 Antenna Embedded Element Patterns

The translation symmetry between identical CBF group pairs has been exploited in Sec. 3.1 to rapidly fill the reduced matrix, but can also be used to efficiently compute the array (element) far-field patterns $\{\mathbf{E}^{\text{far}}, \mathbf{H}^{\text{far}}\}$. Upon denoting the far-field patterns of the Q CBFs by $\{\mathbf{E}_q^{\text{far, CBF}}, \mathbf{H}_q^{\text{far, CBF}}\}$, for $q = 1, \dots, Q$, the total far field patterns can be expanded in terms of these Q CBF patterns as (see also [7, 26]):

$$\{\mathbf{E}^{\text{far}}(\theta, \phi), \mathbf{H}^{\text{far}}(\theta, \phi)\} = \sum_{q=1}^Q I_q^{\text{CBF}} \{\mathbf{E}_q^{\text{far, CBF}}(\theta, \phi), \mathbf{H}_q^{\text{far, CBF}}(\theta, \phi)\} \quad (25)$$

where I_q^{CBF} is the q th expansion coefficient for the q th CBF current. The coefficient vector \mathbf{I}^{CBF} is computed via the CBFM for a certain array excitation.

The approach outlined above is time-consuming if Q , the total number of CBFs, is larger than the number of array elements times the number of excitation schemes considered. However, because many of the subdomains support the same set of CBFs, the respective CBF patterns are identical as well, apart from a phase correction due to their translated position. Hence, translation symmetry can be exploited to compute the patterns pertaining to a few unique sets of CBFs only. For instance, we can write

$$\{\mathbf{E}_p^{\text{far, CBF}}, \mathbf{H}_p^{\text{far, CBF}}\} = \{\mathbf{E}_q^{\text{far, CBF}}, \mathbf{H}_q^{\text{far, CBF}}\} e^{-jk(\mathbf{r}_{pq} \cdot \hat{\mathbf{r}}(\theta, \phi))} \quad (26)$$

where the p th CBF pattern is derived from the q th one by accounting for the translation vector \mathbf{r}_{pq} . The unit vector $\hat{\mathbf{r}}(\theta, \phi)$ denotes the direction of observation, and k is the wavenumber of the homogenous medium. Note that, for our example (Fig. 4), we need to explicitly compute the CBF patterns for the sets of CBFs supported only by the subdomains 1, 3 and 5. The remaining CBF patterns are simply obtained via translation.

5 Multilevel CBFM

The multilevel version of the CBFM (MLCBFM) naturally extends the range of applicability of the monolevel CBFM discussed thus far; it enables one to solve larger problems in almost the same amount of time and for a similar RAM usage [20, 27].

The MLCBFM is a straightforward generalization of the monolevel CBFM, which has been outlined in Sec. 2.1. With a slight change in notation, the full size moment matrix equation (1), at level 0, now reads

$$\mathbf{Z}^{[0]} \mathbf{I}^{[0]} = \mathbf{V}^{[0]} \quad (27)$$

where the uncompressed system matrix $\mathbf{Z}^{[0]}$ is of size $N^{[0]} \times N^{[0]}$. The $N^{[0]} \times 1$ column vector $\mathbf{I}^{[0]}$ holds the (RWG) expansion coefficients for the current, and $\mathbf{V}^{[0]}$ is the excitation vector.

Following the monolevel CBFM, we employ $N^{[1]}$ CBFs at level 1, so that the reduced moment matrix equation becomes

$$\mathbf{Z}^{[1]}\mathbf{I}^{[1]} = \mathbf{V}^{[1]}, \text{ where the } \begin{cases} \text{sub-matrix: } \mathbf{Z}_{mn}^{[1]} = \langle \mathbf{J}_m^{[0]}, \mathbf{Z}_{mn}^{[0]} \mathbf{J}_n^{[0]} \rangle \\ \text{sub-vector: } \mathbf{V}_m^{[1]} = \langle \mathbf{J}_m^{[0]}, \mathbf{V}_m^{[0]} \rangle. \end{cases} \quad (28)$$

The matrix block $\mathbf{Z}_{mn}^{[0]}$ contains the interactions between a pair of RWG groups, each of which supports a set of CBFs, e.g., $\mathbf{J}_m^{[0]}$ or $\mathbf{J}_n^{[0]}$, whose columns are the RWG expansion coefficients describing a CBF on that subdomain. The CBF-compressed matrix $\mathbf{Z}^{[1]}$ is of size $N^{[1]} \times N^{[1]}$. Once the solution for $\mathbf{I}^{[1]}$ has been computed, the solution to the original problem, $\mathbf{I}^{[0]}$, can be found by using

$$\mathbf{I}^{[0]} = \sum_{m=1}^{N^{[1]}} I_m^{[1]} \mathbf{J}_m^{[1],\text{CBF}} \quad (29)$$

where $\{\mathbf{J}_m^{[1],\text{CBF}}\}$ are the entire-domain CBFs at level 1. These vectors contain many zeros to make up the expansion coefficient vectors that are of size $N^{[0]} \times 1$. Next, we proceed this successive compression process for higher levels, resulting in the following recursive scheme at level i :

$$\mathbf{Z}^{[i]}\mathbf{I}^{[i]} = \mathbf{V}^{[i]}, \text{ where the } \begin{cases} \text{sub-matrix: } \mathbf{Z}_{mn}^{[i]} = \langle \mathbf{J}_m^{[i-1]}, \mathbf{Z}_{mn}^{[i-1]} \mathbf{J}_n^{[i-1]} \rangle \\ \text{sub-vector: } \mathbf{V}_m^{[i]} = \langle \mathbf{J}_m^{[i-1]}, \mathbf{V}_m^{[i-1]} \rangle. \end{cases} \quad (30)$$

where the solution at the lower level $i-1$ is expressed in terms of the solution at level i and its set of CBFs, i.e., we can write $\mathbf{I}^{[i-1]} = \sum_{m=1}^{N^{[i]}} I_m^{[i]} \mathbf{J}_m^{[i],\text{CBF}}$, for $i = 1, 2, \dots$

It is to be noted that a set of CBFs need to be generated at each level, and this requires additional operations in comparison with a monolevel CBFM. In conclusion, the number of unknowns may be significantly reduced, but the speed advantage becomes only apparent for electrically large problems [20]. The numerical results section includes the challenging problem of a large array of disjoint subarrays, where RWGs are employed at the lowest level, after which a set of CBFs is employed per antenna element at level 1, and where a set of CBFs is employed per subarray at level 2. We then solve the problem at level 2, and obtain the currents at the lowest level by using the recursive scheme in (30).

6 Numerical Results

The following CBFM computations have been carried out on a 64 bit (x86-64) Linux – openSUSE (v.11.4) server equipped with 2 Intel Xeon E5640 CPUs operating at 2.67 GHz (each CPU has 4 cores/8 threads), with access to 144

GB RAM memory and 2 TB harddisk space. The HFSS simulations were performed on a 64 bit Windows XP server equipped with 2 Intel Xeon 5130 CPUs operating at 2 GHz (each CPU has 2 cores/2 threads), 8 GB RAM, and 300 GB harddisk space.

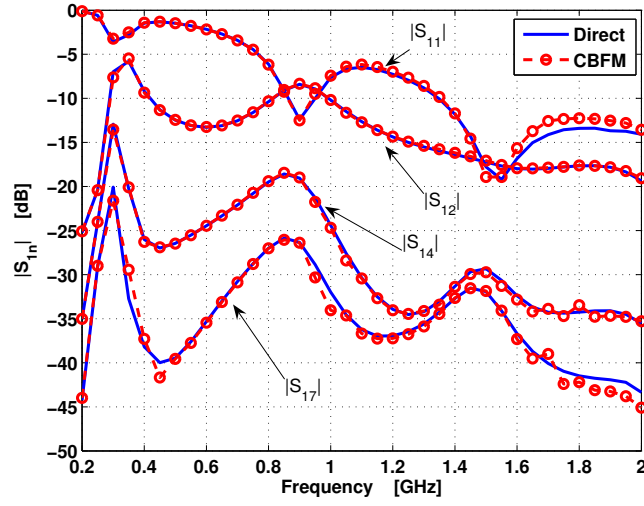
6.1 A 7×1 (Vivaldi) Tapered Slot Antenna Array

The numerical accuracy of the CBFM combined with the ACA will be assessed in this section for a 1-D singly-polarized array of electrically interconnected TSA elements³. The results are compared to a direct MoM solution employing RWG basis functions only. The CBFs are generated as described in Sec. 2.2, where a threshold of 10^{-2} is used both for the SVD procedure in CBFM and the ACA algorithm. The radius for generating the secondary CBFs has been chosen equal to the width of two elements, and has been specified to be independent of the frequency. Following the SVD procedure, only 3 CBFs are retained for the outer two corner elements and 5 CBFs for the inner elements (@ 900 MHz). Figs. 5 and 6 show the computed results for a 7×1 array of TSAs.

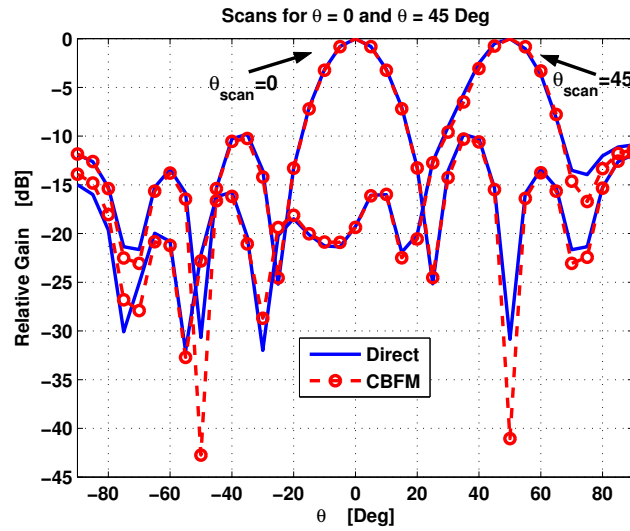
In Fig. 5, one visually observes a very good agreement between the CBFM and direct solution for both the radiation and impedance characteristics. These results show that the electrical interconnection between TSA elements is treated accurately, even though small differences are noticeable in the error surface current distribution $\mathbf{J}_S^{\text{Error}}$ [Fig. 6(b), top]. However, $\|\mathbf{J}_S^{\text{Error}}\|_2$ is at least 30 dB lower than the largest magnitude observed in $\|\mathbf{J}_S^{\text{MoM}}\|_2$, which is found to be ~ 12 dBA/m. The current is a smoothly varying function across the common edge connecting both the element under excitation (#1) and its direct adjacent element (#2), whereas the current continuity degrades across common edges for elements farther out. This can be understood by realizing that CBFs have been generated to accurately represent the current on the excited element as well as on those elements that are directly adjacent (see generation of CBFs in Section 2.2). The all-excited array case demonstrates therefore a better continuity of the current across all the common edges. To reduce the error for the one-element excitation case, more CBFs need to be generated to represent the rapidly varying current on the TSA elements farther out, at the cost of sacrificing the total execution time.

Fig. 6(b) (bottom) illustrates the average error of the RWG expansion coefficients as a result of comparing the CBFM solution to a direct MoM solution. This error is plotted as a function of frequency and refers to the case that corner element 1 is excited by a voltage source while all others are short-circuited; it is defined as

³ The accuracy of a more practical microstrip-fed 8×7 dual-polarized TSA array is discussed in [23], which involves a combination of electrodynamic and quasi-static field models [16].



(a)



(b)

Fig. 5 (a) Scattering parameters S_{1n}^{ant} , for $n = 1, 2, 4, 7$ over frequency for a 150Ω port termination, computed by a direct approach (solid blue line) and CBFM (dashed red line with circles). (b) The relative total gain patterns for two E -plane scans: 0 degrees (broadside scan); and 45 degrees (150Ω port termination). The solid blue line corresponds to the pattern (@ 900 MHz) computed by a direct MoM approach and the pattern in red (dashed with circles) refers to the CBFM solution.

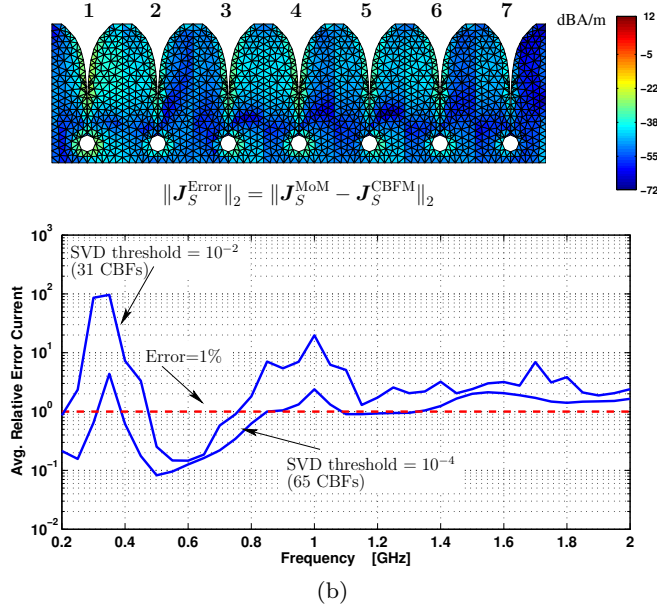
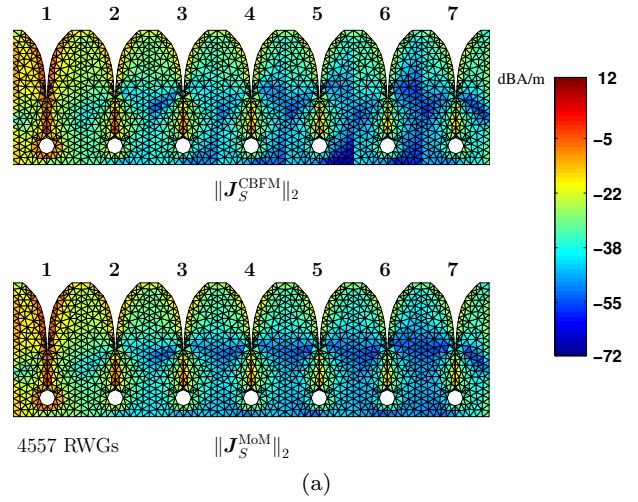


Fig. 6 (a) Magnitude of the normalized surface current distribution in [dBA/m] and port/element numbering for the direct solution and CBFM solution when element 1 is excited by a voltage source and all other terminals are short-circuited (@ 900 MHz). The difference between both current distributions is shown in (b), top, and the average error between the RWG expansion coefficients over frequency is shown in (b), bottom.

$$\text{Rel. Error} = \frac{\sqrt{\sum_{n=1}^N |I_n^{\text{RWG,MoM}} - I_n^{\text{RWG,CBFM}}|^2}}{\sqrt{\sum_{n=1}^N |I_n^{\text{RWG,MoM}}|^2}} \times 100\%. \quad (31)$$

On average, the relative error is less than 5% but may become larger as it tends to oscillate in accordance with the resonant behavior of the surface current. Obviously, near such a resonance, a small shift in frequency may result in a large relative error of the surface current. Resonances appear at almost constant intervals and weaken in strength as the array becomes electrically large, resulting in a relative error that levels out below 5%. For completeness, we also plot the reduced error curve when the SVD threshold is lowered to 10^{-4} . A close inspection of the corresponding current distribution reveals that the current improves globally, which also mitigates the problem of discontinuous behavior of the current across the common edges (although not shown).

6.2 CBFM – ACA Hybridization Results

We consider the computational complexities of both the CBFM and CBFM + ACA approaches for analyzing large arrays of electrically interconnected TSA elements. The total CPU time required to compute the antenna impedance matrix of 2-D single-polarized arrays, ranging from 16 up to 400 TSA elements, is displayed in Table 1. The total CPU time includes the time to generate primary and secondary CBFs, to perform the SVD, to construct and solve the reduced matrix equation, either with or without the ACA algorithm, and to compute the antenna impedance matrix. The total number of matrix blocks \mathbf{Z}_{pq} that need to be constructed remains relatively low. In fact, for a 400 element TSA array, 400×400 blocks need to be constructed but this quantity is reduced to only 1199 (0.7%) by exploiting reciprocity and translation symmetry. Moreover, this number scales as $\mathcal{O}(N)$, where N is the total number of TSA elements. Hence, for relatively small arrays, a large portion of the time is devoted to the generation of CBFs, which implies that the speed advantage of the ACA algorithm becomes more apparent for very large arrays, or for arrays that exhibit little translation symmetry. Due to the fine geometrical features of a TSA element, as well as the utilized method to generate CBFs (primaries+secondaries), the reduction factor of unknowns is quite significant (~ 135).

For ease of comparison of the computational cost of CBFM to that of the combined CBFM–ACA approach, the results of Table 1 have been graphically illustrated in Fig. 7. For the array configurations and sizes that we have

Table 1 Total CPU time required to compute the port impedance matrix of various 2-D single-polarized TSA arrays (@ 900 MHz).

No. TSAs	CBFM [sec.]	CBFM+ ACA [sec.]	No. $\mathbf{Z}_{pq}^{\text{RWG}}$	No. RWGs	No. CBFs
4×4	457	341	54	10380	112
6×6	743	393	150	23418	264
8×8	1160	445	294	41688	480
10×10	1738	537	486	65190	760
12×12	2500	684	726	93924	1104
14×14	3476	934	1014	127890	1512
16×16	4666	1280	1350	167088	1984
18×18	6136	1787	1734	211518	2520
20×20	8022	2527	2166	261180	3120

studied it is concluded that a combined CBFM–ACA approach approximately halves the total execution time with respect to a straightforward CBFM approach.

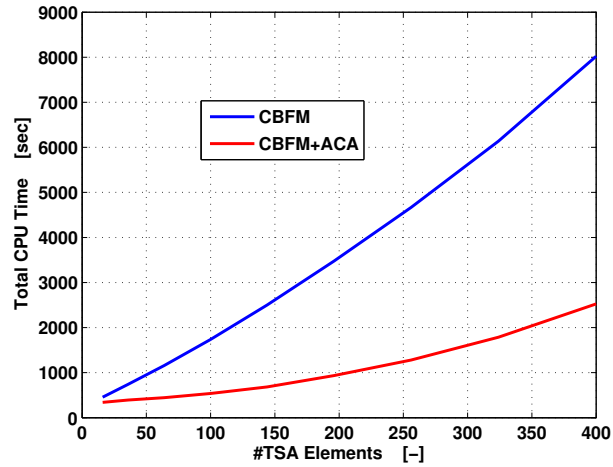


Fig. 7 Total CPU time as a function of the total number of TSA elements for various 2-D array sizes.

Fig. 8 illustrates the corresponding coupling effect and magnitude of the surface current distribution (logarithmic scale) of a 20×20 TSA array when the four center elements are excited while the other ports are short-circuited.

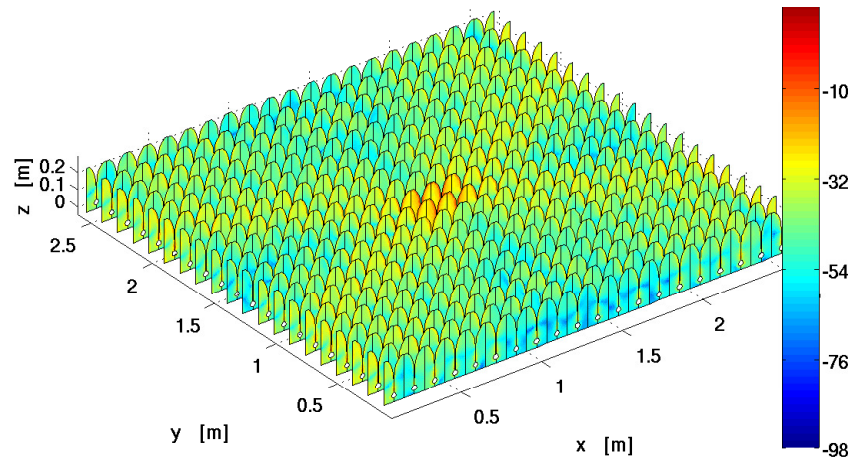


Fig. 8 Surface current distribution of a 20×20 TSA array (Magnitude in [dBA/m] @ 900 MHz). The four center elements are equally excited by voltage generators (1 V) while the others are short-circuited.

6.3 Multilevel CBFM – Array of Subarray Antennas

It is conjectured that the solution for the current on the array of M disjoint subarrays can be accurately synthesized by those found on a single isolated subarray. If a single isolated subarray consists of N antenna elements, we first excite the N elements sequentially and compute the associated subarray currents using a monolevel CBFM approach to generate CBFs (level 1). Afterwards, these solutions so obtained/generated, are used as a set of primary CBFs to synthesize the current distribution on each of the M disjoint subarrays (level 2). Hence, at the highest level we only have to solve for $M \times N$ unknown CBF expansion coefficients (per excitation), as opposed to the $M \times K$ CBFs that would be required for a monolevel CBFM (with $K \gg N$), where K is the total number of CBFs needed to synthesize the current on a single subarray (level 1).

The numerical accuracy and efficiency of a two-level CBFM approach, relative to a monolevel one, will be evaluated in this section for an array of 25 disjoint subarrays of 64 TSA elements each. These gaps may need to be introduced for servicing purposes, so that the individual subarrays can be installed and/or removed as modular units. Furthermore, the transport and manufacturability of relatively small units may offer an advantage. Additionally, an accurate analysis of these nested antenna arrays is important as well, since the gaps/slots between disjoint subarray tiles tend to resonate and lead to anomalous antenna impedance effects as discussed in [36, 37].

Numerical computations have been performed for an SVD threshold level of 10^{-2} (used to reduce and retain a minimal set of basis function at each level

of the MLCBFM). The ACA threshold, which is used to rapidly construct the low-rank (off-diagonal) moment matrix blocks, has been set to 10^{-3} . Numerical experiments have shown that a reduced ACA threshold level has a positive effect on the symmetry of the input impedance matrix. Furthermore, it suppresses the spurious ripples that the element radiation patterns may exhibit, albeit at a cost of longer matrix fill-time. At level 1, the radius for generating the secondary CBFs has been taken equal to the width of two antenna elements, whereas it has been enlarged at level-2 to incorporate all the surrounding subarrays. We have also studied the case in which we bypass the generation of secondary CBFs at level-2.

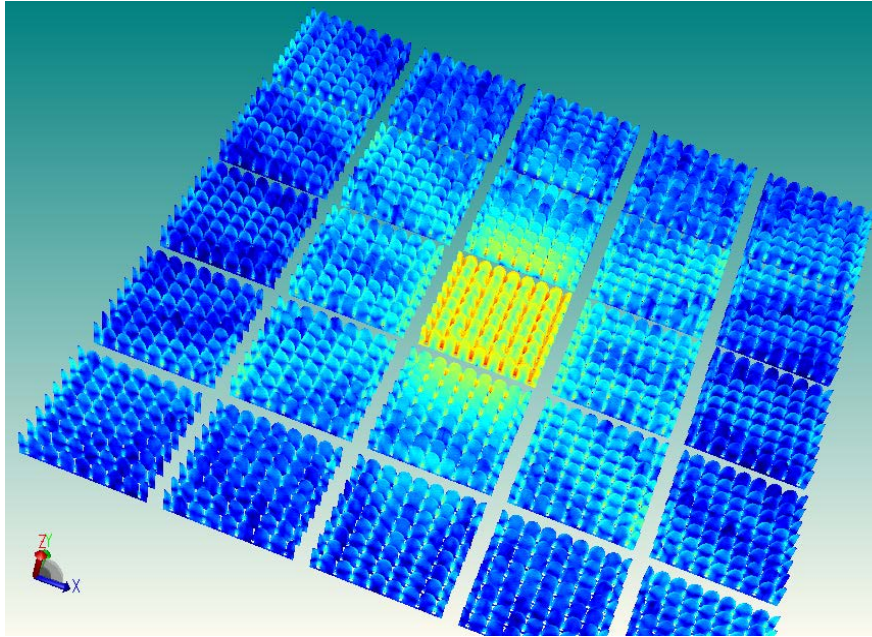


Fig. 9 Array of 25 subarrays (5×5), each of them composed of 64 TSA elements (8×8). To illustrate coupling effects, the active antennas within the central tile are excited by a voltage-gap generator placed over the slot of each TSA element. The central tile scans to broadside (end-fire direction), whereas the TSAs of the surrounding tiles are short-circuited. The magnitude of the surface current distribution is shown on a log scale (80 dB dynamic range).

To illustrate the application of the multilevel CBFM, we now consider a very large antenna array, one that can no longer be solved by using the monolevel CBFM; it consists of 25 subarrays, each comprising of 64 TSA elements (see Fig. 9). The problem requires more than one million RWG basis functions (at level 0, *cf.* Table 2), and the number of level-1 CBFs exceed 10000. The problem has been solved in-core through standard Gaussian elim-

ination techniques at level-2, where the number of CBFs is as low as 3100. The total execution time is just over 11 hours, most of which is devoted to filling the blocks of the moment matrix. Approximate times for assembling the reduced matrix was ~ 176 min; computing the reduced set of excitation vectors ~ 103 min; solving the reduced matrix at level-2 (3100×3100) and computing the antenna impedance matrix ~ 22 min, and the remaining time has been spent on the generation of the primary and secondary CBFs. It is worthwhile to point out that the mesh generation took only 18 min and 9 sec, because advantage was taken of the fact that a large degree of translation symmetry exists at all levels for regularly-spaced antenna arrays.

Table 2 Required computational resources and execution time for a level-2 CBFM approach.

# RWGs (level-0)	# CBFs (level-1)	# CBFs (level-2)	# MoM blocks	# MoM Blocks (Using Symmetry and Reciprocity)	Time to Build MoM Blocks	Total Execution Time
1042200	12000	3100	2560000	14574	323m 55s	667m 33s

6.4 A Metamaterial-Based Gap Waveguide

Recently, a novel class of low-loss low-cost waveguide and transmission-line technologies have been introduced to anticipate to future demands in high-frequency electronics. These structures utilize periodic structures for guiding the fields along desired paths, while incorporating filtering mechanisms and transitions to other waveguides and/or transmission lines at the same time. Furthermore, they allow for a high degree of integration with active electronic components. One of the most profound examples are the recently invented Substrate Integrated Waveguide (SIW, [5]) and Gap Waveguide structures [17]. We will focus on the latter one, whose basic structure consists of a pair of perfect electric conducting (PEC) top and bottom ground planes in conjunction with a periodic texture of metallic objects synthesizing the metamaterial. Fig. 10 depicts the so-called groove gap waveguide [28], where two coaxial probes are used to excite the waveguide fields. The groove is bordered by only a few rows of pins which prevent the fields from leaking out (sideways), provided that we operate in the stop band. The pins are electrically interconnected to the bottom PEC plate, while no electrical contact between the pins and the upper PEC plate is required. The above capacitive gap in the so-called “gap waveguide” not only emulates a perfect magnetic conductor (PMC) boundary condition, but represents a mechanical advantage as well.

As explained above, the CBFM is an enhancement technique for the method of moments and is very well suited to deal with large periodic struc-

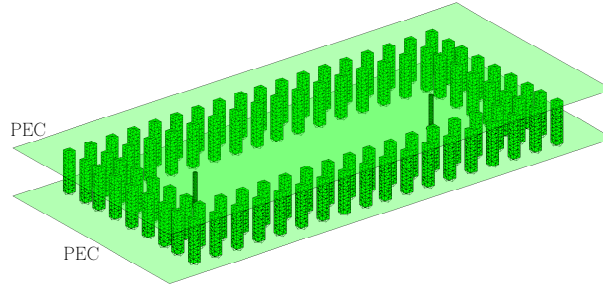


Fig. 10 Coaxial-probe excited groove gap waveguide.

tures in a computationally efficient manner. Furthermore, in Sec. 2.1 we observed that the CBFM operates on the matrix equation without requiring knowledge about the specific type of basis functions, integral equation operators, or Green's functions used. For the fast analysis of gap waveguides, we therefore use the CBFM as an enhancement technique for the MoM approach that employs the parallel-plate Green's function [42]. Consequently, we will only need to discretize and solve for the electric currents on the pins and probes in Fig. 10.

In regard to the configuration shown in Fig. 11, the parallel-plate Green's function computation illustrates that a dipole point source can have an x -, y -, or z -orientation (or linear combinations thereof) inside a parallel-plate region. After application of the image principle, the EM field is regarded as being radiated by two superimposed 1D-line arrays of dipole point sources with the original and possibly mirrored polarization. Each line array has an inter-dipole spacing of twice the plate distance: $2d$. In Dyadic form, the spatial parallel-plate Green's function \mathbf{G} is expressed as $\mathbf{G}(\mathbf{r}, \mathbf{r}') = G_{xx}^N \hat{\mathbf{x}}\hat{\mathbf{x}}^T + G_{yy}^N \hat{\mathbf{y}}\hat{\mathbf{y}}^T + G_{zz}^N \hat{\mathbf{z}}\hat{\mathbf{z}}^T$, where

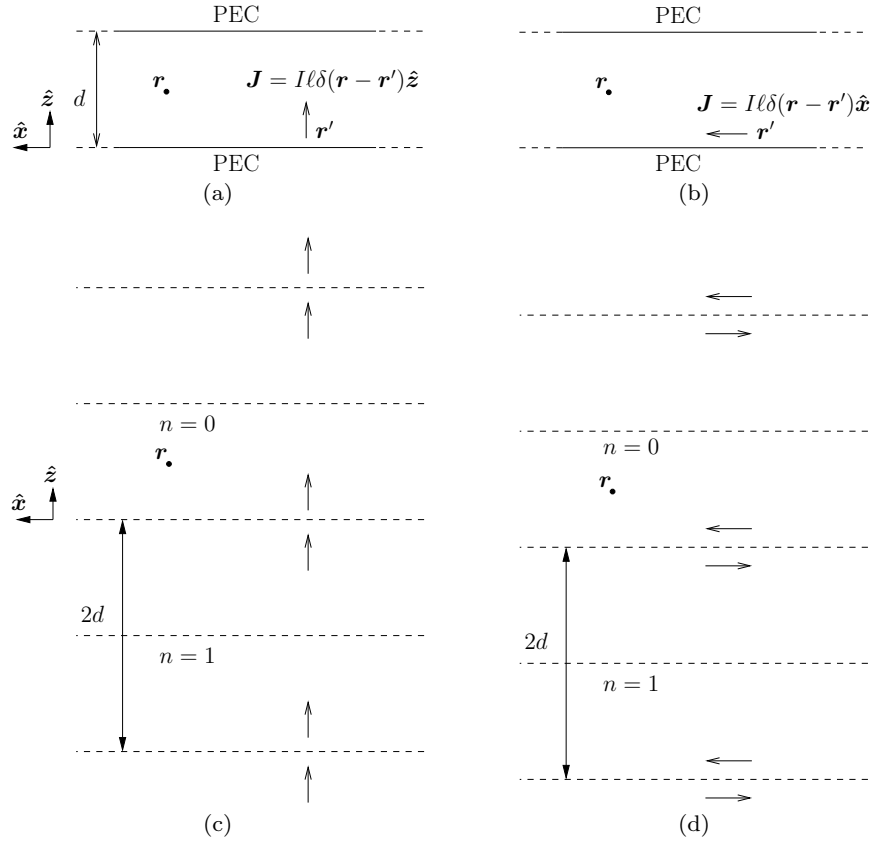


Fig. 11 (a) z -polarized and (b) x -polarized electric Hertzian dipole currents in between two infinitely large parallel PEC plates separated by a distance d ; (c) and (d), the repeated application of the image principle for both dipole polarizations, respectively.

$$\begin{aligned}
 G_{xx}^N &= \sum_{n=-N}^N \frac{e^{-jk_0 \sqrt{\rho^2 + (z-z'+2dn)^2}}}{4\pi \sqrt{\rho^2 + (z-z'+2dn)^2}} \\
 &\quad - \sum_{n=-N}^N \frac{e^{-jk_0 \sqrt{\rho^2 + (z+z'+2d(n-1))^2}}}{4\pi \sqrt{\rho^2 + (z+z'+2d(n-1))^2}} \\
 G_{yy}^N &= G_{xx}^N \\
 G_{zz}^N &= \sum_{n=-N}^N \frac{e^{-jk_0 \sqrt{\rho^2 + (z-z'+2dn)^2}}}{4\pi \sqrt{\rho^2 + (z-z'+2dn)^2}} \\
 &\quad + \sum_{n=-N}^N \frac{e^{-jk_0 \sqrt{\rho^2 + (z+z'+2d(n-1))^2}}}{4\pi \sqrt{\rho^2 + (z+z'+2d(n-1))^2}}
 \end{aligned} \tag{32}$$

for $N \rightarrow \infty$, and where $\rho^2 = (x - x')^2 + (y - y')^2$. The spatial summations in Eq. (32) are known to be slowly convergent, however, each summation can be computed rapidly using the Shanks transformation [38]. This method is easy to implement and very fast if only a few digits of accuracy is required, which is sufficient in most practical cases [42]. For example, when considering the new series $G_{xx}^1, G_{xx}^2, \dots$, the Shanks-extrapolated value for G_{xx}^∞ is

$$G_{xx}^\infty \approx \frac{G_{xx}^{N+1}G_{xx}^{N-1} - (G_{xx}^N)^2}{G_{xx}^{N+1} - 2G_{xx}^N + G_{xx}^{N-1}} \quad (33)$$

where N is taken sufficiently large. Numerical experiments show that the best trade-off between the solution accuracy and the total series evaluation time is to use the doubly repeated Shanks transformation, which only requires $N \approx 5$ terms [42].

The electric surface currents on the pins and coaxial probes, of the guiding structure shown in Fig. 10, are expanded in terms of 37088 RWG basis functions. The CBFs are generated only for a single pin and for the coaxial probe. As an example, consider Fig. 12(a), where the CBFs are generated for a pin in isolation by employing 382 RWGs. We let a PWS be incident on the pin with angular increments of $\Delta\theta^i = \Delta\phi^i = 90^\circ$ (and two polarizations), which generates 16 currents. The generated pin currents are stored as RWG expansion coefficients vectors and make up the columns of the matrix $\mathbf{J}_q = \mathbf{U}\mathbf{D}\mathbf{Q}^H$, where the right-hand side is the SVD of \mathbf{J}_q [see also Eq. (8)]. The magnitude of the normalized singular values in \mathbf{D} are plotted in Fig. 12(a). With an appropriate thresholding procedure on the singular values, only the first 12 column vectors of the left-singular matrix \mathbf{U} are retained, and subsequently used as CBFs. The reduction in the number of unknowns per pin is therefore $382/12=31.8$ (@ 12 GHz). We exploit the translation symmetry to generate a set of CBFs for all the pins, since the set of CBFs is identical for each pin, and since this allows also for a rapid construction of the reduced matrix (see Sec. 3.1). A similar CBF generation procedure is followed for the coaxial probes.

After all the pins and probes support a set of CBFs, the reduced moment matrix equation $\mathbf{Z}^{\text{red}}\mathbf{I}^{\text{CBF}} = \mathbf{V}^{\text{red}}$ is constructed, where \mathbf{V}^{red} is a result of exciting the structure by impressed magnetic frill currents that are supported by the coaxial apertures.

The remaining geometrical dimensions of the groove gap waveguide are as described in Fig. 12(b). Additionally, the radius and length of the coaxial probes are 0.25 and 5 mm, respectively, and the parallel-plate separation distance $d = 7.25$ mm.

To examine the numerical accuracy, the 100-Ohm S -parameters for the gap waveguide structure in Fig. 12(b) have been computed through both CBFM and the HFSS software. In HFSS, the adaptive meshing terminates if the relative field error is less than 1%. The computed S -parameters for CBFM and HFSS are shown in Fig. 13 and are seen to be in good agreement.

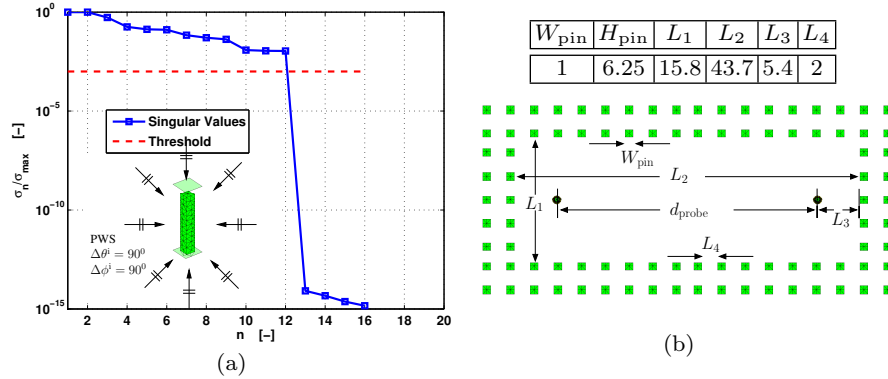


Fig. 12 (a) Generation of CBFs on a pin using a plane wave spectrum (PWS). The singular value spectrum is shown where a threshold is used to limit the maximum number of employed CBFs. (b) Geometrical dimensions of the Groove gap waveguide in [mm].

The solve times for this relatively small problem is 1 min. 41 sec. and 1 min. 24 sec. for CBFM and HFSS, respectively. The simulation times are comparable due to the relatively large overhead needed by the CBFM to determine the CBFs. The CBFM employed 1112 CBFs (37088 RWGs), while HFSS employed 42158 tetrahedra. Owing to the nature of the array structure, the meshing time is only 5 sec. for the CBFM, while it takes 3 min. 57 sec. for HFSS.

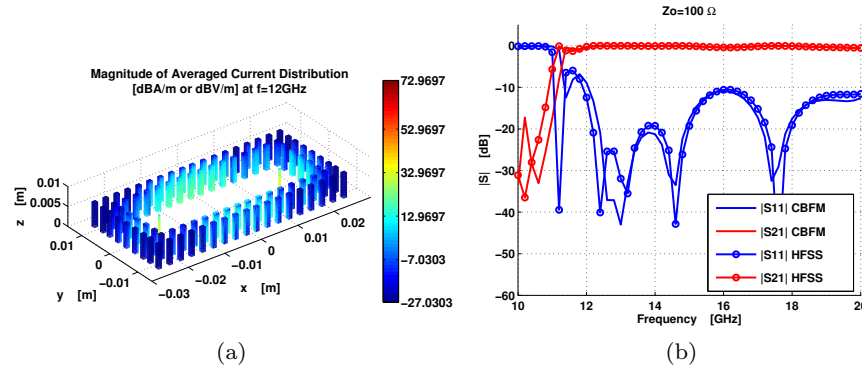


Fig. 13 (left) the magnitude of the computed electric current and S -parameters of a groove gap-waveguide when excited by a pair of coaxial probes; (right) the numerical results are computed by the CBFM employing the parallel-plate Green’s function. The numerically computed results are validated through the HFSS software.

Next, by changing L_2 one can examine the total solve time as a function of the problem size. The results are shown in Fig. 14, where the scaling of

the solve time for CBFM outforms that of HFSS by about a factor of three. Also, for equal simulation times, the problem size for CBFM can be about twice larger than for the HFSS software. The HFSS software could not handle problems for $d_{\text{probe}} > 1.3$ m, due to memory constraints for that server. The non-gradual increase in simulation time is caused by the adaptive meshing of HFSS.

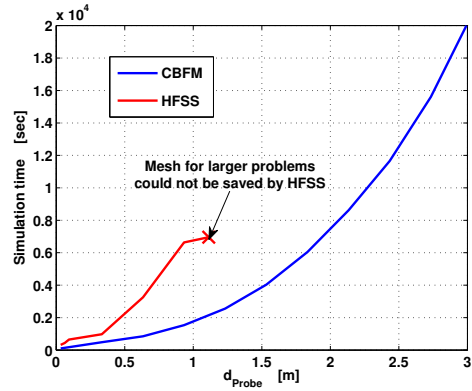


Fig. 14 Scaling of the method: the total solve time as a function of problem size (d_{probe}).

7 Summary

The Characteristic Basis Function Method (CBFM) is an enhancement technique for the method-of-moments for solving large scattering and radiation problems. This chapter describes a specific version of the CBFM, namely one that is tailored to analyze large periodic structures, including antenna arrays and metamaterial-based waveguides. The Characteristic Basis Functions (CBFs) are generated numerically, and only for a few elementary building blocks, which are then used to rapidly generate sets of CBFs throughout the entire array lattice. This method is capable of generating CBFs for electrically interconnected array elements by letting sets of CBFs partially overlap, since this preserves the continuity of the surface current across subdomain boundaries when synthesizing the final solution for the current. Once each subdomain within the array lattice supports a set of CBFs, the CBF interactions are computed to construct the reduced moment matrix. To expedite the matrix filling process, an approach has been described to exploit the translation symmetry between set pairs of CBFs within the array structure. A further reduction of the matrix fill-time is realized through the application of

the Adaptive Cross Approximation (ACA) algorithm. Finally, to be able to analyze extremely large nested array structures, a multilevel version of the monolevel CBFM is described for achieving an even higher compression of the reduced moment matrix.

The numerical results demonstrate that the solutions for the antenna array current, the antenna input impedance matrix, and the radiation characteristics are in very good agreement with those obtained by using a direct MoM approach, while the reduction factor in the number of basis functions for a monolevel CBFM approach – relative to a direct MoM approach – are significant, i.e., typically two-to-three orders in magnitude. The CBFM can be explained as an algebraic method for solving large matrix equations and, hence, does not depend on the nature of the Green's function. This has been demonstrated for a metamaterial-based gap waveguide analyzed through a MoM approach employing the parallel-plate Green's function. Very large gap waveguides are analyzed, those that are far beyond the reach of commercially available software codes, such as HFSS, without comprising the solution accuracy much, as demonstrated for smaller more tractable problems.

References

1. Bebendorf, M.: Approximation of boundary element matrices. *Numer. Math.* **86**(4), 565–589 (2000)
2. Bekers, D.J., van Eijndhoven, S.J.L., van de Ven, A.A.F., Borsboom, P.P., Tjihuis, A.G.: Eigencurrent analysis of resonant behavior in finite antenna arrays. *IEEE Trans. Microw. Theory Tech.* **54**(6), 2821–2829 (2006)
3. Bleszynski, E., Bleszynski, M., Jaroszewicz, T.: AIM: Adaptive integral method for solving large-scale electromagnetic scattering and radiation problems. *Radio Sci.* **31**(5), 1225–1251 (1996)
4. Boryssenko, A.O.: private communication (2004)
5. Bozzi, M., Georgiadis, A., Wu, K.: Review of substrate-integrated waveguide circuits and antennas. *Microwaves, Antennas & Propagation, IET* **5**(8), 909–920 (2011)
6. Çivi, O.A., Pathak, P.H., Chou, H.T., Nepa, P.: A hybrid uniform geometrical theory of diffraction – moment method for efficient analysis of electromagnetic radiation/scattering from large finite planar arrays. *Radio Sci.* **35**(2), 607–620 (2000)
7. Craeye, C.: A fast impedance and pattern computation scheme for finite antenna arrays. *IEEE Trans. Antennas Propag.* **54**(10), 3030–3034 (2006)
8. Craeye, C., Tjihuis, A.G., Schaubert, D.H.: An efficient MoM formulation for finite-by-infinite arrays of two-dimensional antennas arranged in a three dimensional structure. *IEEE Trans. Antennas Propag.* **51**(9), 2054–2056 (2003)
9. Delaunay, B.: Sur la sphère vide. *Izvestia Akademii Nauk SSSR, Otdelenie Matematicheskikh i Estestvennykh Nauk* **7**, 793–800 (1934)
10. Delgado, C., Catedra, M.F., Mittra, R.: Efficient multilevel approach for the generation of characteristic basis functions for large scatters. *IEEE Trans. Antennas Propag.* **56**(7), 2134–2137 (2008)
11. Garcia, E., Delgado, C., de Adana, F.S., Catedra, F., Mittra, R.: Incorporating the multilevel fast multipole method into the characteristic basis function

- method to solve large scattering and radiation problems. In: Proc. IEEE AP-S International Symposium, pp. 1285–1288. Honolulu, Hawaii (2007)
12. Golub, G.H., van Loan, C.F.: Matrix Computations. 3rd ed. Baltimore, MD: Johns Hopkins, London (1996)
 13. Harrington, R.F.: Time-Harmonic Electromagnetic Fields. McGraw-Hill Book Company, New York and London (1961)
 14. Harrington, R.F.: Field Computation by Moment Methods. The Macmillan Company, New York (1968)
 15. Heinstadt, J.: New approximation technique for current distribution in microstrip array antennas. *Micr. Opt. Technol.* **29**, 1809–1810 (1993)
 16. Ivashina, M.V., Redkina, E.A., Maaskant, R.: An accurate model of a wide-band microstrip feed for slot antenna arrays. In: Proc. IEEE AP-S International Symposium, pp. 1953–1956. Hawaii, USA (2007)
 17. Kildal, P.S., Alfonso, E., Valero-Nogueira, A., Rajo-Iglesias, E.: Local metamaterial-based waveguides in gaps between parallel metal plates. *IEEE Antennas Wireless Propag. Lett.* **8**(1), 84–87 (2009)
 18. Kurz, S., Rain, O., Rjasanow, S.: The adaptive cross-approximation technique for the 3-D boundary-element method. *IEEE Trans. Magn.* **38**(2), 421–424 (2002)
 19. Lancellotti, V., de Hon, B.P., Tijhuis, A.G.: An eigencurrent approach to the analysis of electrically large 3-d structures using linear embedding via green’s operators. *IEEE Trans. Antennas Propag.* **57**(11), 3575–3585 (2009)
 20. Laviada, J., Las-Heras, F., Pino, M.R., Mittra, R.: Solution of electrically large problems with multilevel characteristic basis functions. *IEEE Trans. Antennas Propag.* **57**(10), 3189–3198 (2009)
 21. Lu, W.B., Cui, T.J., Qian, Z.G., Yin, X.X., Hong, W.: Accurate analysis of large-scale periodic structures using an efficient sub-entire-domain basis function method. *IEEE Trans. Antennas Propag.* **52**(11), 3078–3085 (2004)
 22. Maaskant, R.: Analysis of large antenna systems. Ph.D. thesis, Eindhoven University of Technology, Eindhoven (2010). URL <http://alexandria.tue.nl/extra2/201010409.pdf>
 23. Maaskant, R., Ivashina, M.V., Iupikov, O., Redkina, E.A., Kasturi, S., Schaubert, D.H.: Analysis of large microstrip-fed tapered slot antenna arrays by combining electrodynamic and quasi-static field models. *IEEE Trans. Antennas Propag.* **56**(6), 1798–1807 (2011)
 24. Maaskant, R., Mittra, R., Tijhuis, A.G.: Application of trapezoidal-shaped characteristic basis functions to arrays of electrically interconnected antenna elements. In: Proc. Int. Conf. on Electromagn. in Adv. Applicat. (ICEAA), pp. 567–571. Torino (2007)
 25. Maaskant, R., Mittra, R., Tijhuis, A.G.: Fast analysis of large antenna arrays using the characteristic basis function method and the adaptive cross approximation algorithm. *IEEE Trans. Antennas Propag.* **56**(11), 3440–3451 (2008)
 26. Maaskant, R., Mittra, R., Tijhuis, A.G.: Fast solution of multi-scale antenna problems for the square kilometre array (SKA) radio telescope using the characteristic basis function method (CBFM). *Applied Computational Electromagnetics Society (ACES) Journal* **24**(2), 174–188 (2009)
 27. Maaskant, R., Mittra, R., Tijhuis, A.G.: Multilevel characteristic basis function method (MLCBFM) for the analysis of large antenna arrays. Special Section on Computational Electromagnetics for Large Antenna Arrays, *The Radio Science Bulletin* **336**(336), 23–34 (2011)
 28. Maaskant, R., Takook, P., Kildal, P.S.: Fast analysis of gap waveguides using the characteristic basis function method and the parallel-plate green’s function. In: Proc. Int. Conf. on Electromagn. in Adv. Applicat. (ICEAA), pp. 788–791. Cape Town (2012)

29. Matekovits, L., Laza, V.A., Vecchi, G.: Analysis of large complex structures with the synthetic-functions approach. *IEEE Trans. Antennas Propag.* **55**(9), 2509–2521 (2007)
30. Matekovits, L., Vecchi, G., Bercigli, M., Bandinelli, M.: Synthetic-functions analysis of large aperture-coupled antennas. *IEEE Trans. Antennas Propag.* **57**(7), 1936–1943 (2009)
31. Matekovits, L., Vecchi, G., Dassano, G., Orefice, M.: Synthetic function analysis of large printed structures: the solution space sampling approach. In: *Proc. IEEE AP-S International Symposium*, pp. 568–571. Boston, Massachusetts (2001)
32. Mittra, R., Ma, J.F., Lucente, E., Monorchio, A.: CBMOM—an iteration free MoM approach for solving large multiscale em radiation and scattering problems. In: *Proc. IEEE AP-S International Symposium*, pp. 2–5. Washington DC (2005)
33. Neto, A., Maci, S., Vecchi, G., Sabbadini, M.: A truncated Floquet wave diffraction method for the full wave analysis of large phased arrays – part ii: Generalization to 3-D cases. *IEEE Trans. Antennas Propag.* **48**(3), 601–611 (2000)
34. Prakash, V., Mittra, R.: Characteristic basis function method: A new technique for efficient solution of method of moments matrix equations. *Micr. Opt. Technol.* **36**, 95–100 (2003)
35. Rao, S., Wilton, D., Glisson, A.: Electromagnetic scattering by surfaces of arbitrary shape. *IEEE Trans. Antennas Propag.* **30**(3), 409–418 (1982)
36. Schaubert, D.H., Boryszenko, A.O.: Subarrays of Vivaldi antennas for very large apertures. In: *Proc. 34th European Microwave Conference*, pp. 1533–1536. Amsterdam (2004)
37. Schaubert, D.H., Kasturi, S., Elsallal, M.W., van Cappellen, W.A.: Wide bandwidth Vivaldi antenna arrays – some recent developments. In: *Proc. European Conference on Antennas and Propag. (EuCAP)*, pp. 1–4. Nice, France (2006)
38. Shanks, D.: Non-linear transformation of divergent and slowly convergent sequences. *J. Math. Phys.* **34**, 1–42 (1955)
39. Skrivervik, A.K., Mosig, J.R.: Analysis of finite phased arrays of microstrip patches. *IEEE Trans. Antennas Propag.* **41**(9), 1105–1114 (1993)
40. Stevanovic, I., Mosig, J.R.: Subdomain multilevel approach with fast MBF interactions. In: *Proc. IEEE AP-S International Symposium*, pp. 367–370. Monterey, California (2004)
41. Suter, E., Mosig, J.R.: A subdomain multilevel approach for the efficient MoM analysis of large planar antennas. *Micr. Opt. Technol.* **26**(4), 270–277 (2000)
42. Takook, P., Maaskant, R., Kildal, P.S.: Comparison of parallel-plate greens function acceleration techniques. In: *Proc. European Conference on Antennas and Propag. (EuCAP)*, pp. 1–5. Prague, Czech Republic (2012)
43. Tiberi, G., Monorchio, A., Manara, G., Mittra, R.: Hybridizing asymptotic and numerically rigorous techniques for solving electromagnetic scattering problems using the characteristic basis functions (CBFs). In: *Proc. IEEE AP-S International Symposium*, pp. 22–27. Columbus, Ohio (2003)
44. Tomasic, B., Hessel, A.: Analysis of finite arrays – a new approach. *IEEE Trans. Antennas Propag.* **47**(3), 555–564 (1999)
45. Trefethen, L.N., Bau, D. (eds.): *Numerical Linear Algebra*. Society for Industrial and Applied Mathematics (SIAM), Philadelphia (1997)
46. Vandenbosch, G.A.E., Demuynck, F.J.: The expansion wave concept – part ii: A new way to model mutual coupling in microstrip arrays. *IEEE Trans. Antennas Propag.* **46**(3), 407–413 (1998)
47. Vandenbosch, G.A.E., Van de Cappelle, A.R.: Use of combined expansion scheme to analyze microstrip antennas with the method of moments. *Radio Sci.* **27**(6), 911–916 (1992)
48. Vita, P.D., Freni, A., Matekovits, L., Pirinoli, P., Vecchi, G.: A combined AIM-SFX approach for large complex arrays. In: *Proc. IEEE AP-S International Symposium*, pp. 3452–3455. Honolulu, Hawaii (2007)

49. Yeo, J., Prakash, V., Mitra, R.: Efficient analysis of a class of microstrip antennas using the characteristic basis function method (CBFM). *Micr. Opt. Technol.* **39**, 456–464 (2003)
50. Zhao, K., Vouvakis, M.N., Lee, J.F.: The adaptive cross approximation algorithm for accelerated method of moments computations of EMC problems. *IEEE Trans. Electromagn. Compat.* **47**(4), 763–773 (2005)